DISCRETE WHEEL TOPOLOGY MODELED USING TENSEGRITY MECHANICS

A Thesis

by

CALEB HAMILTON PECK

Submitted to the Office of Graduate and Professional Studies of
Texas A&M University
in partial fulfillment of the requirements for the degree of

MASTER OF SCIENCE

Chair of Committee,	Manoranjan Majji
Committee Members,	Robert Skelton
	Aniruddha Datta
Head of Department,	Rodney Bowersox

August 2020

Major Subject: Aerospace Engineering

ABSTRACT

In an effort to expand the breadth of tensegrity geometries, novel discrete toroidal topologies are developed, analyzed and presented. The scope of this thesis encompasses the complete design formulation of the connectivity of these structures, computation of the static equilibrium equations to confirm the pre-stressability, dynamic analysis of the steady-state rolling of the three bar wheel, and the examination of the 3D Michell truss force distribution and minimum material volume un-der a single bending load. The major contributions of this work are the design of a new tensegrity toroid, based on a basic three-bar prism, and the extension of the planar Michell truss into three dimensional space. Mechanical analysis of these new structures is performed using a comprehen-sive software package which solves for the static and dynamic equations under the assumptions of tensegrity mechanics. The results demonstrate the new toroid is stable under pre-stress and models a continuum toroid as the complexity of the structure reaches infinity. The new 3D Michell topol-ogy is also stiff and may be designed to resist bending loads with minimum material volume. The design and analysis of these new structures forms the foundation further research into practical application can build upon.

DEDICATION

To Charles, Isabelle, Frank, and Mary Jo for their unwavering support of higher education.

ACKNOWLEDGMENTS

I would like to thank Dr. Skelton for the inspiring discussions, Dr. Majji for his mentorship, and Dr. Datta for his support. Also, Joe Peterson for many sanity checks, Davis Adams for several reviews, and, of course, Madeline for her love and wisdom.

CONTRIBUTORS AND FUNDING SOURCES

Contributors

This work was supported by a thesis committee consisting of Professor Manoranjan Majji (advisor) and Robert Skelton of the Department of Aerospace Engineering and Professor Aniruddha Datta of the Department of Electrical Engineering.

All other work conducted for the thesis was completed by the student independently.

Funding Sources

Graduate study was supported by a Graduate Research Assistantship from Texas A&M University partially funded by the National Geospatial Intelligency Agency, Grant Number HM04761912015 and the Office of Naval Research, Grant Number N00014-19-1-2435.

TABLE OF CONTENTS

Page

LIST OF FIGURES

FIGURE Page

1. INTRODUCTION TO TENSEGRITY AND TENSEGRITY MECHANICS

1.1 Tensegrity History

In the late 1940's, a new type of free floating sculpture was gaining popularity. The, somewhat controversial, origin of these structures dates to the constructivism work of Latvian Karlis Johansons in the 1920's [2, 3]. However, it achieved wide-spread notice through the works of Kenneth Snelson [4, 5, 6] in the 1940's. His sculptures were made of rigid bodies that seemed to be suspended in air via a network of taut cables. While the artwork was championed by Snelson, Buckminster Fuller received his own patent for this kind of structure and coined the term *Tensegrity* [7, 8]. This word is a combination of *tension* and *integrity* since the tension in the strings is what keeps the multi-body system rigid. This state defines a class of structures that are *pre-stressable*, such that the structure is in a state of equilibrium when there are no external forces and all cables are in tension [9, 10]. This quality is a prime advantage because the stiffness of the structure is easily tuned by modifying the stress in the members [11]. Another unique property of tensegrity is that the external shape can change without changing the stiffness. Conversely, the stiffness may also change without changing the external shape [12].

As Fuller eloquently describes in his patent, tensegrity structures are "islands of compression in a sea of tension" [13]. The 'islands' are the rigid bodies, like bars or rods, while the sea of tension is formed by a network of tensile members such as strings or cables. For some time, this work was appreciated as art but dismissed by structural engineers. Later, in the 1970's, tensegrity structures began to attract the attention of the science community [14, 7] which sought to rigorously define, explore, and utilize the extraordinary properties of these structures. Work by Sultan, Motro, Skelton, and many others followed to compound the research on this paradigm of structural mechanics centered around the concept of pre-stressability [15, 16, 17, 18, 19, 20]. Over the last couple decades, applications and research of tensegrity structures has ranged from bio-mechanics [21], smart sensors [22], controlled structures [23, 24], deployable structures [25, 26, 27] and large

frames [12].

Throughout its genesis, many definitions of tensegrity have been developed and modified [14, 28, 29]. The body of this work will adhere to the definition by Skelton [12] which first defines a *tensegrity configuration* as:

Let a set of rigid bodies in a specific configuration have torque-less connections (i.e. ball-joints). Then this grouping forms a tensegrity configuration if it can be stabilized by some set of internal tensile members connected between the rigid bodies.

From this definition, a *tensegrity system* is composed of a given set of strings connected to a *tensegrity configuration* of rigid bodies that stabilizes the configuration [12]. Indeed, a tensegrity system can be stable or unstable depending on the connectivity of the strings; however, by definition, a stabilizing string connectivity must exist for a configuration to be defined. Thus, a tensegrity structure for this work is a collection of straight, uniaxially loaded compression and tension members in a state of self-equilibrium with friciton-less connections. According to Skelton, the *class-k* of a tensegrity is defined by the maximum number of bars that meet at any given joint. So, for a class-1 structure, there are no bars that touch. A class-2 structure contains nodes at which two bars meet, and so on. The condition of uni-axial loading is significant because it assumes that no member is to experience bending stresses. This remarkable simplification ushers the way for a new method of structural mechanics that allows tensegrity to be modeled accurately without the need of finite element methods.

Inspired by Snelson's sculptures, early work in tensegrity systems began with exploring new geometries that fall into this structural paradigm [14]. Early works introduced various basic polyhedra such as: the Simplex [15], Saddle-Vertical-Diagonal (SVD) structures [30], 3-Bar Prism, and many geodesic shapes [31]. Over time, these prisms evolved into geometric classes of structures, for example: cylinders, spheres [32], towers [33], and domes [34]. However, there is still a great amount of work to be done to design, characterize, and analyze new tensegrity topologies [11]. Of these topologies, toroidal (donut-like) shapes have only recently become a focus for form finding and investigation. Emmerich *et al* investigated a connected loop of simplex structures that

fashioned into a toroid [17]; however, it was Yuan that formally introduced a toroid using n class-1 prisms consisting of m bars each [35]. Every two segments of this torus is the same. Thus, cyclic repeatability is possible by rotating the segment $\frac{4\pi}{n}$ times and connecting the new segment with the previous. This type of toroid was updated by Xu who added the possibility of overlapping between adjacent segments [36]. Nagase and Skelton derived a Double Helix Tensegrity structure (DHT) [37] that offers a general connectivity pattern which can be formed into various prism geometries such as cylinders, toroids, and spheres. A class-2 toroid, proposed by Lu, is based on a half-octahedron prism consisting of 4 struts and 12 cables, which is modified from its planar form to a trapezoid that offers a more general toroidal shape [38]. The work presented herein introduces a class-2 tororidal topology that is composed of repeated, askew 3-bar prisms stabilized by 12 strings each. Global buckling of the toroid is prevented by connecting additional strings between each of the prisms. A central bar is used, but not required, as a central hub to which a group of these stabilizing strings may be attached, akin to the spokes of a bicycle wheel. Adhering to the assumption of straight bars, a minimum of three prisms is required to form a loop. The geometry of this new toroid is defined by 7 parameters, which inherently defines the geometry of the base prism. The novelty of this toroid is its design application of a wheel, contrary to previous toroidal applications of dome-like structures. Such application inspired placing rigid members in a configuration that is in the direction of the reaction forces with the ground.

1.2 Why Tensegrity?

Beyond the tunability of a structure's stiffness, tensegrity structures are also mass efficient. Members need only be placed in the path of a load [39], therefore a cleverly designed tensegrity topology can limit the number of members required to support such a load. Additionaly, mass is optimized by using analytical solutions to compute the minimum material volume of each member with respect to a material's ultimate yield and buckling strength [12]. This method offers the ability to design structures that can achieve minimum mass under a given external loading condition. Skelton has proved that tensegrity is the optimal-mass solution to many of the fundamental static loading conditions (compression, tension, buckling, simply supported, torsion). Of specific interest

for this work is the discrete two-dimensional Michell truss, which is an optimal-mass structure to support single bending loads [1]. Given specific loading conditions, the sign of the force (i.e. tension or compression) for each member is known. This condition offers a direct application for tensegrity structures since each member can be assigned as bar or string given the loading condition. The efforts of this present work is to extend this 2D structure out of the plane and introduce a topology that supports out-of-plane forces.

A key quality of many of the prism geometries that formed the foundation of scientific research into tensegrity was the ability to repeat base prisms to form large, stiff structures. More interestingly, the contour of these large structures can be morphed by changing the lengths of some, or all, of the members that make up the prisms [24, 26]. In fact, it is possible for the prisms to maintain equilibrium as their shapes change as long as the control is slow and within what is known as an 'equilibrium manifold' [19]. The manipulation of these structures is rather efficient because motion of the structure is a result of the axial length changes of individual members. Thus, through harmonizing all of the member controls, large topological changes can be made to the while ensuring stiffness is maintained. Tensegrity, then, is a viable solution to the problem of building large space frames that can be stowed during launch. Deployable structures require large deformations from the original, stored configuration which often involves many moving parts operating at a high complexity. These structures are typically designed with motors at each pivot point that requires enough torque to move not only the members directly attached to it, but any subsequent member beyond that. The position of the motors create severe moments on the pivot joint and, consequently, larger motors are required to provide sufficient torque in response to those moments. Tensegrity avoids this issue because the deformation of the topology is done by re-orienting the system to a new equilibrium position through the manipulation of member lengths. Similar to tendons found in animals and humans, the forces applied to rotate a rigid member of a system about one end are applied at the opposite end of the member, providing the largest moment arm possible for rotation. This means the reorientation of a tensegrity is significantly more efficient than traditional robotic manipulators, which presents the capability of a whole new class of deployable space structures

[27]. Furthermore, mass efficieny is a supreme motivation in space operations since the dollor cost of launching objects is on the order of 10s of thousands of dollars per kilogram [40].

1.3 Reinventing the Wheel

Unstructured terrain presents a challenge for the drive systems of space vehicles that are designed to travel across extraterrestrial environments. While sensor suites can detect large obstacles and slopes, it is often the case that soil depth, hardness, and composition within a local region is varying. These variations of ground condition demand that the drive system of a vehicle must be robust to such changes and reliably provide traction. The application of the 3-bar toroid as a wheel is modeled and analyzed under the paradigm of tensegrity mechanics. The results of these models highlight the advantages of applying tensegrity mechanics to this class of structure, rather than other methods such as finite element analysis.

The first wheeled vehicle used in space exploration was the Soviet remote-controlled robot, Lunokhod [41]. The robot landed in November of 1970 with a mission design of 90 days. The durability of the robot extended the mission to 11 months, during which the robot traveled throughout the Sea of Rains. The proximity of the Moon from the Earth allowed for near real-time operation of the robot, which followed a "move and wait" technique in which the operator would command a steering angle and move the robot one wheel circumference forward. One year later, the Lunar Rover Vehicle (LRV) was flown during the Apollo 15 mission. This vehicle was designed to carry astronauts and equipment across the lunar terrain at speeds of up to 14 km/hr, and boasts the interplanetary land speed record of 17 km/hr [41, 42]. Multiple, extensive studies were conducted during the decade prior to its first mission to determine the best choice of wheels for the rover [43]. The final choice was a weave of zinc-coated piano wire with an aluminum hub, each weighing roughly 5.5 kg. This wheel was chosen for its overall compromise between weight, comfort, and soft ground performance.

Mars presented much different challenges to roving vehicles compared to the Moon. The vast increase in distance from Earth required innovations in autonomous vehicle control such that the rover could manage navigation itself, rather than wait for a command signal from Earth. A cul-

mination of struggles in developing large, autonomous vehicles changed the paradigm of Martian exploration to a micro-rover. The first autonomous vehicle to touchdown and operate on Mars was the 10.5 kg Pathfinder Microrover known as Sojourner; operating for 83 Sols after it landed on Mars on July 4, 1997 [44, 45]. Often in history, successful exploration missions are the catalyst for further exploration ventures. The success of Sojourner and validation of its control system spurred the development of rovers Spirit and Opportunity [46] and Curiosity. Now, the Mars 2020 rover will soon attempt to join the ranks of successfully landed missions and further push the boundaries of understanding of the Red Planet. One thing in common with all of these unmanned systems: they drive. The same way that we change our tires according to season or the intention to drive on highways or off-road, so too must rovers use the proper drive systems demanded by their extraterrestrial environment.

Currently there are numerous projects involving the locomotion of manned and un-manned vehicles. A survey conducted in 2014 by Flessa et. al reviewed the status of planetary exploration rovers [47]. The study concluded a base-line drive system consisting of four to six wheels, all wheel drive with selected wheel steering, and passive kinematic suspension. Each of the NASA rover missions used a rigid wheel design with compliant spokes. The ExoMars rover developed by the European Space Agency spurred developments in flexible wheel technologies [48]. These types of wheels were first proposed during the LRV research but were eventually not chosen for the final design. Recent research in flexible wheels introduce new methods in modeling and validating wheel designs with respect to the shape of flexible members, number of grousers, and their angles [49, 50]. Further, models of the terra-mechanic interactions with wheels continue development and are verified through experimental testing [51, 52]. These works may be utilized to further advance rover mobility design and expand the working envelope of navigable terrains. Doing this would widen the possibilities of rover exploration in diverse terrain, but also increase the robustness of autonomous vehicle movement such that these robots may travel to regions of unknown surface composition.

While terrain navigation is an application, the motivation for this work is to develop new tenseg-

rity topologies with initial static and dynamic analysis. Investigations into discrete toroidal topologies are conducted to discover possible structures to replace typical continuum wheels found on most space vehicles. Because of the discrete nature of these structures, tensegrity mechanics is the proper method to describe, model, and analyze these structures. This work presents a new tensegrity toriod that is designed to support ground reaction forces while rolling down an incline with no slip. The toroid is designed by tessalating a base prism, the non-minimal 3-bar prism, in a loop and appling extra strings to resist global buckling. The deficiency of the 3-bar prism to support bending forces led to the design of a new topology that extended the capability of the mass-optimal discrete Michell truss. A recursive method of joints is used to determine *a priori* the member force directions which can pre-determine the member type required to form a stable tensegrity.

The scope of this thesis covers two major contributions: (1) The parameterization of the 3-bar toroid's design, and static and dynamic analysis of the wheel using a tensegrity modeling code developed by Goyal et. al [53]. (2) The introduction of a new spatial prism to support bending loads, formed from the mass-optimal discrete Michell truss. The next chapter of this thesis summarizes tensegrity dynamics; Chapter 3 presents the topology and dynamic model of the novel 3-bar tensegrity wheel. Chapter 4 begins with the 2D Michell truss and the baseline parameters that form the foundation for the new spatial truss. The topology and analysis of the 3D Michell Truss begins in Section 4.2. Finally, an exploration into another wheel topology is discussed in chapter 5.

2.1 Dynamics of a Single Rigid Bar

The derivation of the equations of motion of a tensegrity structure begins with the dynamics of a single rigid bar of length l. The orientation of the bar in the inertial frame is described by the vector $\mathbf{b} = \mathbf{n}_j - \mathbf{n}_i$. Reiterating the assumptions of tensegrity structures, it is assumed that there are no moments applied about the longitudinal axis of the rod. Further, the generalized external forces are resolved to be located at the terminal points of the rod. The governing equations of rotational and translational motion of a single rigid bar of mass and length $m_b,\ l_b$, respectively, are summarized by the equations [54]

$$J\ddot{\mathbf{b}} = \frac{1}{2}\left(\mathbf{f}_2 - \mathbf{f}_1\right) - \frac{1}{2l^2}\mathbf{b}\mathbf{b}^T\left(\mathbf{f}_2 - \mathbf{f}_1\right) - \frac{J}{l^2}\mathbf{b}\dot{\mathbf{b}}^T\dot{\mathbf{b}} \tag{2.1}$$

$$m_b\ddot{\mathbf{r}} = \mathbf{f}_1 + \mathbf{f}_2 \tag{2.2}$$

Where $\mathbf{r}$ is the inertial position vector of the center of mass of the rod and $\mathbf{f}_1, \mathbf{f}_2$ are force vectors applied to each end of the bar shown in Figure (2.1).

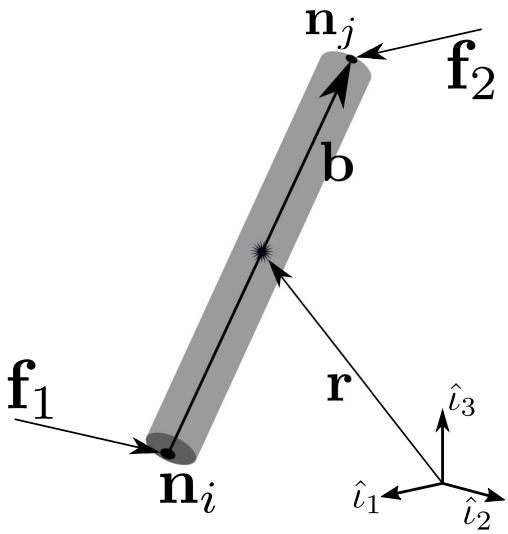

Figure 2.1: Single Tensegrity Bar Vector

2.2 Tensegrity Connectivity

Typically, the dynamics of a multibody system are formulated such that the collection of vector equations for each body is concatenated to form a single vector equation of the system [55]. The dynamics of a tensegrity system, however, may be formed in a simpler structure by describing the dynamics in a matrix form. A tensegrity structure is founded on connections of compressive and tensile members, and the location of these intersections are called nodes. For a general tensegrity system consisting of n nodes in 3D space, the node matrix, N, is a $(3 \times n)$ matrix such that the i^{th} column of node matrix defines the inertial position components of the i^{th} node, $\mathbf{n}_i$. Given β bars and α strings, the 'connectivity' of the bar and string members are described by matrices dubbed the bar connectivity matrix, C_b of size $(\beta \times n)$, and string conenctivity matrix, C_s of size $(\alpha \times n)$. These matrices consist of elements $(0, 1, -1)$ that specify which nodes are the terminal ends of the member. For example, consider the vector of the k^{th} bar, $\mathbf{b}_k$, that begins at node $\mathbf{n}_i$ and terminates at node $\mathbf{n}_j$. The k^{th} row of C_b contains $+1$ and -1 in the i^{th} and j^{th} column, respectively, with zeroes elsewhere. Thus the vectors describing each bar and string are contained in their respective matrix, B and S. The bar and string matrices can be computed according to the node matrix and the respective connectivity matrices

$$B = NC_b^T \in \mathbb{R}^{3\times\beta} \tag{2.3}$$

$$S = NC_s^T \in \mathbb{R}^{3\times\alpha} \tag{2.4}$$

The collection of position vectors, $\mathbf{r}$ such that $\mathbf{r}_k$ describes the mass center of the k^{th} bar is the matrix R where

$$\mathbf{r}_k = \frac{1}{2}[NC_b^T]_k \tag{2.5}$$

$$= [NC_r^T]_k \tag{2.6}$$

$$R = NC_r^T \tag{2.7}$$

2.2.1 Example: The Planar D-Bar

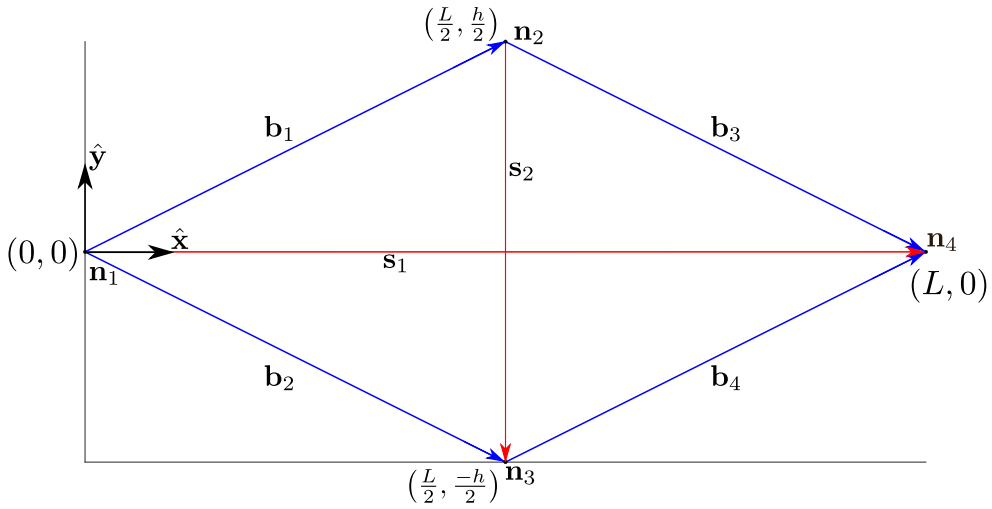

Figure 2.2: 2D D-Bar

To provide an example, consider the planar D-bar shown in Figure (2.2). The blue arrows represent bar members and the red arrows are cables. The positions of the four nodes are collected in the node matrix as:

$$N = \begin{bmatrix} 0 & \frac{L}{2} & \frac{L}{2} & L \\ 0 & \frac{h}{2} & -\frac{h}{2} & 0 \end{bmatrix} \tag{2.8}$$

The truss has four bars and two strings thus, $\beta = 4$ and $\alpha = 2$ and the bar and string connectivity matrices are of size (4×4) and (2×4), respectively.

$$C_b = \begin{bmatrix} -1 & 1 & 0 & 0 \\ -1 & 0 & 1 & 0 \\ 0 & -1 & 0 & 1 \\ 0 & 0 & -1 & 1 \end{bmatrix} \qquad C_s = \begin{bmatrix} -1 & 0 & 0 & 1 \\ 0 & -1 & 1 & 0 \end{bmatrix} \tag{2.9}$$

Then, using equations (2.3), (2.4), the bar and string matricies are

$$B = \begin{bmatrix} \frac{L}{2} & \frac{L}{2} & \frac{L}{2} & \frac{L}{2} \\ \frac{h}{2} & -\frac{h}{2} & -\frac{h}{2} & \frac{h}{2} \end{bmatrix} \qquad S = \begin{bmatrix} L & 0 \\ 0 & -h \end{bmatrix} \tag{2.10}$$

Using these matrices, the geometry and connectivity of any tensegrity is possible no matter the complexity of the structure.

2.3 Matrix Formulation

Considering the node, bar, and string matrices presented in the previous section, the dynamic equations for a full tensegrity system is then [54]

$$\begin{bmatrix} \ddot{B} \\ \ddot{R} \end{bmatrix} \begin{bmatrix} \hat{J} & 0 \\ 0 & \hat{m}_b \end{bmatrix} \begin{bmatrix} C_b \\ C_r \end{bmatrix} + \begin{bmatrix} B \\ R \end{bmatrix} \begin{bmatrix} -\hat{\lambda} & 0 \\ 0 & 0 \end{bmatrix} \begin{bmatrix} C_b \\ C_r \end{bmatrix} = F \tag{2.11}$$

$$\hat{\lambda} = -\hat{J}\hat{l}^2 \lfloor \dot{B}^T \dot{B} \rfloor - \frac{1}{2}\hat{l}^2 \lfloor B^T F C_b^T \rfloor \tag{2.12}$$

Where the hat operator $\hat{[\,]}$ denotes a matrix with the operand on the diagonal and zeros elsewhere. The operator $\lfloor \circ \rfloor$ sets all off-diagonal elements of the square matrix operand to zero. The matrix F is defined such that the k^{th} column of F is the vector sum of all forces applied to node k. Using the definitions of B and R, equation (2.11) can be rewritten in terms of the connectivity matrices, the node positions and its derivatives [54] as

$$\ddot{N}\left(C_b^T \hat{J} C_b + C_r^T \hat{m}_b C_r\right) - N\left(C_b^T \hat{\lambda} C_b\right) = F \tag{2.13}$$

Now, the forces, F, that are exerted on the structure may be decomposed into two groups: internal and external forces. The internal forces are caused by the tensions in the strings and can be described as a 'force density', γ, which is the force normalized by the string member length. Thus, the tension of the k^{th} string is $\mathbf{t}_k = \mathbf{s}_k \gamma_k$. All internal forces can be collected into the matrix TC_s such that the total force matrix is the sum of the external forces into the node, W, and the internal

forces coming out of a node:

$$F = W - TC_s \tag{2.14}$$

$$= W - NC_s^T \hat{\gamma} C_s \tag{2.15}$$

This equation can be substituted back into equation (2.15) to create the compact, non-linear second order matrix differential equations for the rotational and translational dynamics of a class-1 tensegrity system in terms of the node positions [54]

$$\ddot{N}M + NK = W \tag{2.16}$$

$$M = C_b^T \hat{J} C_b + C_r^T \hat{m} C_r \tag{2.17}$$

$$K = C_s^T \hat{\gamma} C_s - C_b^T \hat{\lambda} C_b \tag{2.18}$$

These equations can be applied for class-k structures by convering each class-k joint into k class-1 joints and applying coincident constraints [54]. These constraints are of the form

$$NP = D \tag{2.19}$$

Where P and D are defined such that, n_i and n_j must coincide, the columns of P, D are specified such that $n_i - n_j = 0$. The addition of these constraints adds an extra term in Equation (2.16) and the new equation of motion for the system, given these constraints, is

$$\ddot{N}M + NK = W + \Omega P^T \tag{2.20}$$

Where Ω is a matrix of Lagrange multipliers that satisfy the dynamics and constraints for all time steps. This extra term can be interpreted as the reaction forces required to mantain the coincidence of the k class-1 joints.

3. 3-BAR TENSEGRITY TOROID

A common theme in tensegrity mechanics is utilizing a 'base' prism and tessellating, or repeating, that prism to build larger structures. Tensegrity towers are representative structures of this repeating process, and show that a minimal, deployable structure may be built with simple building blocks [56, 33]. A novel toroid concept is presented which repeats a non-minimal 3-bar prism and then connects the beginning and end node in a loop to close the structure. The emphasis of this topology is the intended ability for the toroid to perform as a vehicle's wheel.

3.1 Non-Minimal 3-Bar Prism

The base unit for this wheel is the non-minimal 3-bar tensegrity prism [57]. The 'minimal' prism, first fashioned by Kenneth Snelson, is also dubbed the "*Snelson Prism*" [58] to honor his discovery of this unique structure. Structural properties of the minimal 9 string configuration are explored in Skelton's book [12] and form the basis for several large space-frame structures composed of this repeated unit. Given bar lengths of equal size, the equilibrium condition of the structure is such that there is a 30 degree twist angle from the orientation of the planar triangle formed by the bottom three nodes and the triangle formed by the top three nodes. This orientation represents a state of self-equilibrium, such that the tension in the structure supports the weight of the structure itself. The prism used in this work is derived from the minimal 9 string prism, but the equal length assumption is removed and more parameters are required to define the geometry than the original four. The addition of 3 extra strings further stiffens the structure. The role of the 3-bar prism is to use two of the bars as contact points with the ground, the "tread", while the third bar connects to the adjacent prisms of the wheel and forms the "rim". Seven geometric parameters are required to describe the wheel completely. These inherently construct the individual 3-bar prism to the proper size/shape in accordance to the toroid parameters. The node positions for a single prism is shown in figure 3.1. Node 6 from one prism is connected to node 3 of the subsequent prism, and this continues until the circuit is completed.

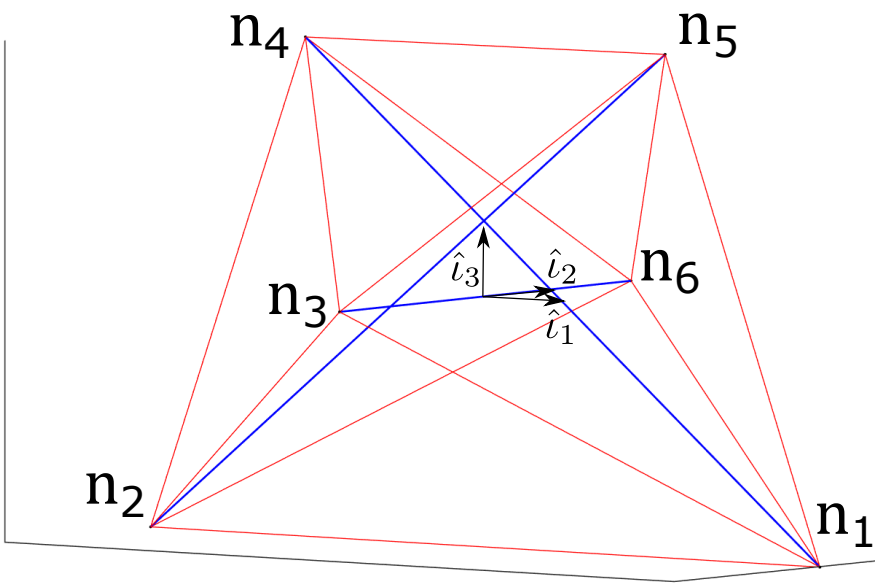

$$\mathbf{n}_1 = \begin{bmatrix} \frac{T}{2} \\ 0 \\ -R_o \end{bmatrix} \qquad \mathbf{n}_2 = \begin{bmatrix} -\frac{T}{2} \\ 0 \\ -R_o \end{bmatrix} \qquad \mathbf{n}_3 = \begin{bmatrix} 0 \\ -R_m \tan\left(\frac{\pi}{n}\right) \\ -R_m \end{bmatrix}$$

$$\mathbf{n}_4 = \begin{bmatrix} -\frac{t}{2} \\ -D \\ -R_i \end{bmatrix} \qquad \mathbf{n}_5 = \begin{bmatrix} \frac{t}{2} \\ D \\ -R_i \end{bmatrix} \qquad \mathbf{n}_6 = \begin{bmatrix} 0 \\ R_m \tan\left(\frac{\pi}{n}\right) \\ -R_i \end{bmatrix}$$

Figure 3.1: 3-Bar Prism Node Positions

A diagram describing the toroid parameters is shown in figure 3.2. The red lines represent strings while the blue lines are the rigid bars.

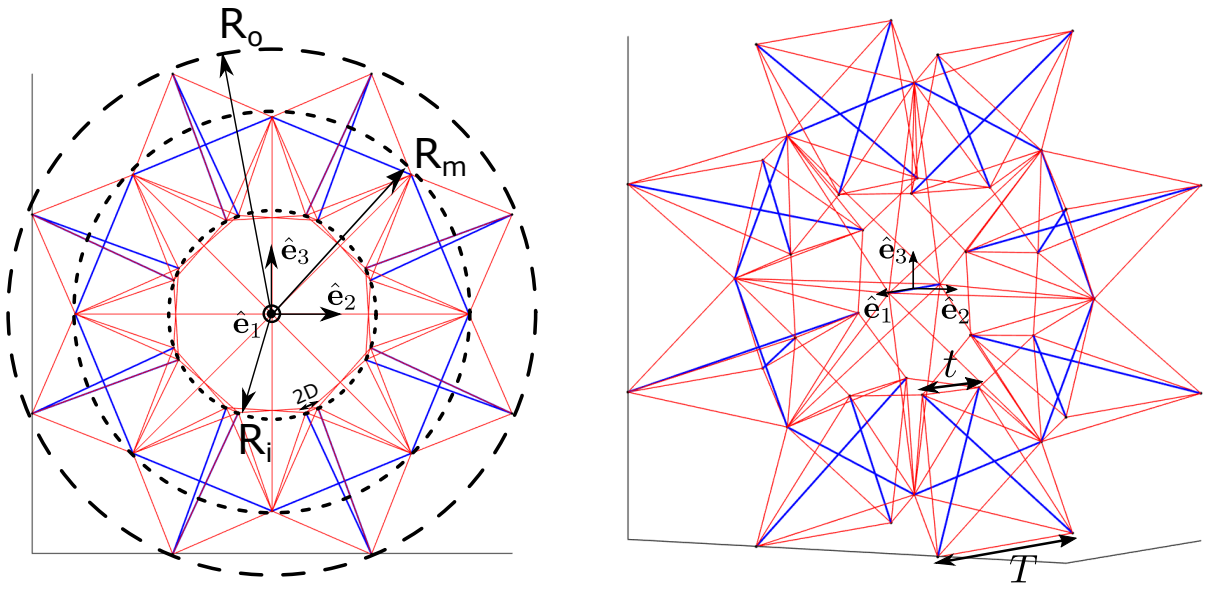

Number of Sides: n Outer Tread Width: T Inner Tread Width: t Tread Offset Distance: D
Outer Radius: R_o Inner Radius: R_i Rim Radius: R_m

Figure 3.2: 3-Bar Toroid Parameters

While each individual segment of the toroid is stiff, the structure as a whole is not stiff until additional strings are included to stabilize the connection points between prisms. The joints at these connections are assumed to be compliant in all directions, therefore a single prism can spin about the axis defined by the bar connecting nodes 3 and 6. This rotation can be restricted by including strings that resist the rotation of the inner and outer tread nodes. There are three methods to do this:

1. Attach a string from the rim nodes to each end of an interior axle, like the spokes of a bicycle wheel.

2. Connect the interior tread nodes of one prism to the interior tread of its two neighbor prisms.

3. Connect the outer tread nodes of one prim to the outer tread of its two neighbors.

Two options listed above must be applied to ensure global stability of the toroid. The combination of the first two options is presented in figure 3.2. The 'spoke' strings maintain the circular

arrangement of each individual prism, while the interior node connections stabilize the rotations that may occur about the axis perpendicular to the plane of rotational symmetry. A collection of all three methods is presented in figure 3.3. The left, middle, and right images are options (1,2), (1,3), and (2,3) respectively. Using the inner and outer connections omits the 'axle' bar and forms the most toroidal looking topology. This is also the least massive solution partly due to the omission of an additional bar. The advantage of this method is that it opens up the space inscribed by the interior tread. An application of this toroidal topology is for locomotion over a surface, which means the wheel would probably be attached to a vehicle through an axle. Also, it is preferred to keep as many members internal to the rim as possible and limit the number of members in contact with the surface. Because of this, the first method was adopted for the following rolling analysis.

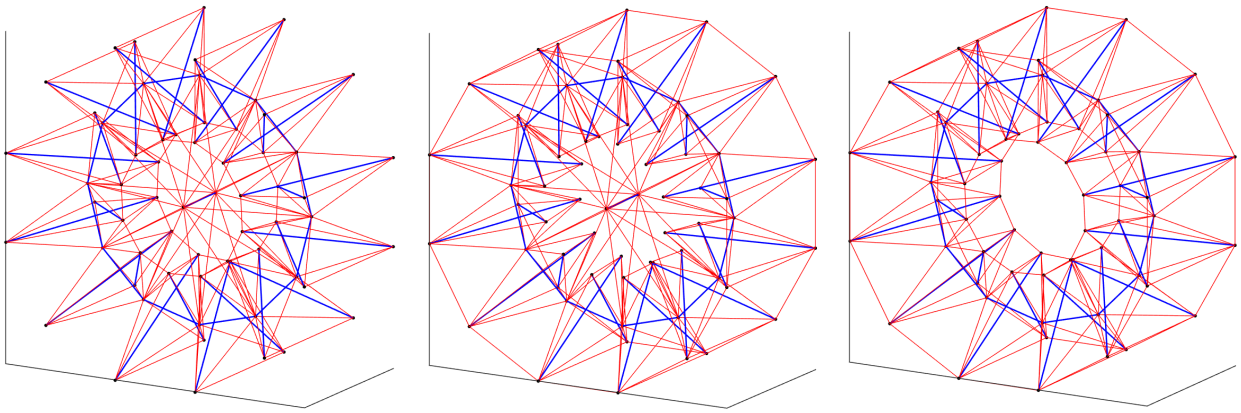

Figure 3.3: 3-Bar Toroid Extra String Options

3.2 Tensegrity Wheel Dynamics

3.2.1 Kinematics

As mentioned previously, this toroid inspires the concept of a novel wheel application for space. Thus, a dynamic analysis was performed to derive the equations of motion for the center of the wheel. Consider the general case of the wheel rolling down an incline, sketched in figure 3.4. At any time there may be zero, one, two pairs of outer tread nodes in contact with the ground. The

rolling will be modeled such that the rotation is planar about the $\hat{\iota}_1$ axis. The downhill pair of nodes is the point of rotation for the wheel, with reaction forces exerted both parallel and perpendicular to the slope. The reaction forces exerted by the ground will be modeled with a damping coefficient c.

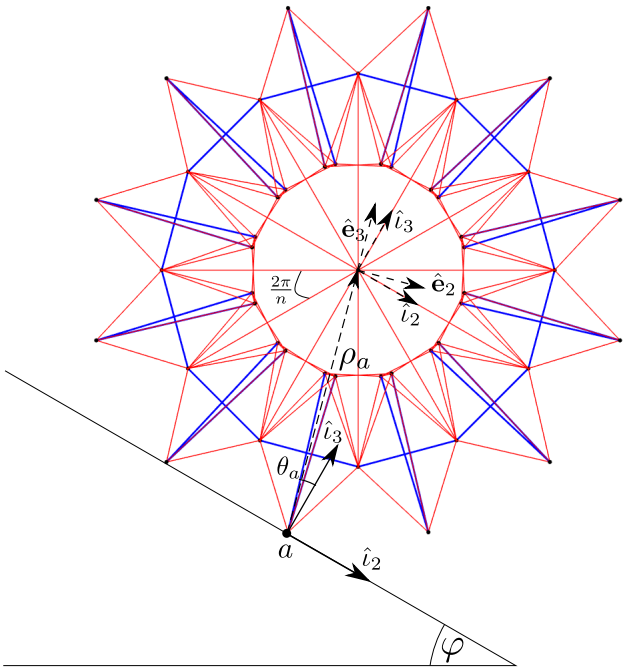

Figure 3.4: Sketch of 3-Bar Tensegrity Wheel Geometry

The inertial coordinate system is located on the incline at the point where the downhill external node first comes in contact with the ground. While $\hat{\iota}_1$ and $\hat{\mathbf{e}}_1$ are aligned, it is convenient to orient the body-fixed coordinate frame such that $\hat{\mathbf{e}}_3$ is aligned with the vector defined by $\rho_a = \mathbf{r}_c - \mathbf{r}_a$. The angle θ_a is then the angle between the $\hat{\iota}_1$ axis and the vector ρ_a. The position vector of the

center of the wheel and its derivatives are then

$$\mathbf{r}_c = r_0 \left(-\sin\theta_a \hat{\iota}_2 + \cos\theta_a \hat{\iota}_3\right) \tag{3.1}$$

$$\dot{\mathbf{r}}_c = \dot{\theta_a} r_0 \left(-\cos\theta_a \hat{\iota}_2 - \sin\theta_a \hat{\iota}_3\right) \tag{3.2}$$

$$\ddot{\mathbf{r}}_c = r_0 \left(\left(\sin\theta_a \dot{\theta_a}^2 - \cos\theta_a \ddot{\theta_a}\right) \hat{\iota}_2 - \left(\cos\theta_a \dot{\theta_a}^2 + \sin\theta_a \ddot{\theta_a}\right) \hat{\iota}_3\right) \tag{3.3}$$

$$\tag{3.4}$$

3.2.2 The External Force Matrix

To simulate the dynamic response of this tensegrity toroid, the reaction forces incident from rolling on an incline are modeled to populate external force matrix W. Then, the external force matrix is used as an input to the node equations of motion derived in section 2.3. Simulating the wheel's motion this way improves the model by incorporating the additional assumptions that are inherent in the tensegrity dynamics formulation. The force matrix W will be composed of the gravitational force and the reaction forces caused by the ground on a pair of contact nodes. Sufficient stiffness of the wheel offers the assumption that the wheel is rigid such that gravity is applied at the center of mass. Due to the symmetry of the wheel, the center of mass is located at the center of the wheel. The ground reaction model includes the normal force, $\mathbf{w}_a$, which is equal and opposite to the gravity force, and reaction forces, $\mathbf{f}_a^T, \mathbf{f}_a^N$, which regulate the velocity of contact nodes to zero. This reaction force is a dynamic function of the contact node velocities and attempts to model the no-slip condition with the ground. Thus, the total reaction force exerted on

the contact pair, a, is $\mathbf{F}_a$ which populates the column of W according to their node index.

$$\mathbf{F}_a = \mathbf{w}_a + \mathbf{f}_a \tag{3.5}$$

$$= \frac{1}{2}\left(mg \begin{bmatrix} 0 \\ -\sin\varphi \\ \cos\varphi \end{bmatrix} + \begin{bmatrix} 0 \\ f_a^t \\ f_a^n \end{bmatrix} \right) \tag{3.6}$$

$$f_a^T = -c\dot{N}(2,a) \tag{3.7}$$

$$f_a^N = -c\dot{N}(3,a) \tag{3.8}$$

$$\tag{3.9}$$

Where $\dot{N}$ is the matrix of the node velocities and m is the mass of the entire wheel. These equations can be substituted into the reaction force equations which are subsequently used to populate the external force matrix W. Then, the dynamic equations for a tensegrity system, equation 2.16 are numerically solved.

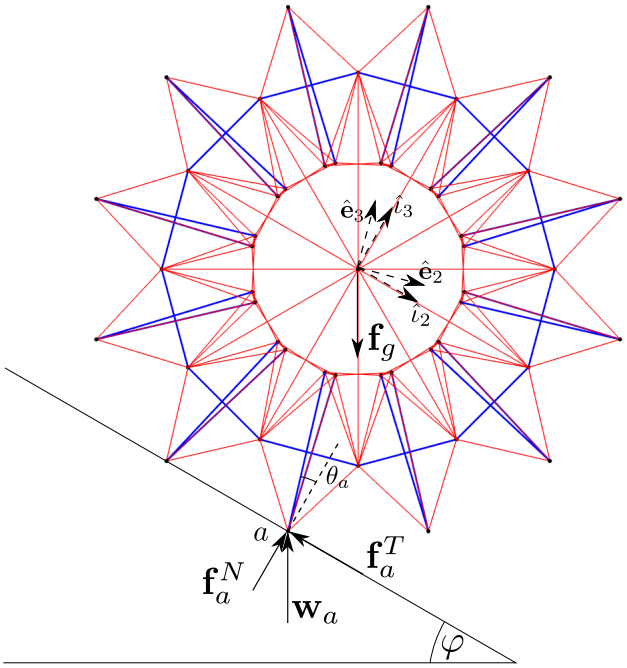

Figure 3.5: 3-Bar Wheel Free Body Diagram

3.2.3 The Inertia Matrix

The wheel is constructed in the tensegrity paradigm, therefore it is inappropriate to assume the inertia is that of a flat disk or cylinder. However, the inertia of the wheel may be derived by computing the inertia of a single slender bar and superimposing each bar's inertia about the wheel's center to form the inertia for the entire wheel.

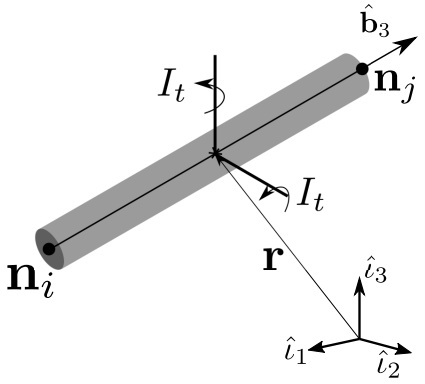

Figure 3.6: Inertia of a Single Bar Member

Consider a single bar member. The bar-fixed axes will be aligned with the principal axes of inertia of a slender rod such that the $\hat{\mathbf{b}}_3$ axis points along the bar vector $\mathbf{b}$, as shown in figure 3.6. Then, the inertia matrix of the k^{th} bar of the wheel, coordinitized in the bar frame, is

$$[{}^k\tilde{\mathbf{I}}_c]^b = \begin{bmatrix} I_t & 0 & 0 \\ 0 & I_t & 0 \\ 0 & 0 & 0 \end{bmatrix} \tag{3.10}$$

For a tensegrity, the inertia about the longitudinal axis is negligible therefore, $I_a = 0$. To calculate the inertia of the entire wheel, it is necessary to translate the bar-centric inertia matrix into the wheel-fixed coordinate frame, $[\hat{\mathbf{e}}_1, \hat{\mathbf{e}}_2, \hat{\mathbf{e}}_3]^T$, see figure 3.7. This is done by rotating the bar

fixed frame to that of the wheel-fixed frame via a rotation tensor, $\mathbf{R}$, such that

$$\hat{\mathbf{e}}_i = \mathbf{R}^T \hat{\mathbf{b}}_i \tag{3.11}$$

$$[^k\tilde{\mathbf{I}}_c]^e = \mathbf{R}\,[^k\tilde{\mathbf{I}}_c]^b\,\mathbf{R}^T \tag{3.12}$$

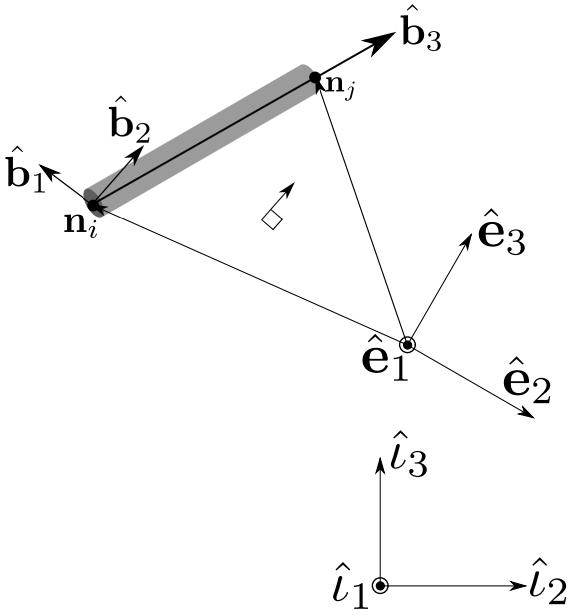

Figure 3.7: Definition of Coordinate Frames

Where $[^k\tilde{\mathbf{I}}_c]^b$ is the inertia of the bar described using components of the bar-fixed frame, and $[^k\tilde{\mathbf{I}}_c]^e$ describes the bar's inertia using components of the wheel-centered frame. The components of the rotation matrix are readily available by componentiating the directions of $\hat{\mathbf{b}}_i$ in the wheel-fixed frame. By this point, the directions of $\hat{\mathbf{b}}_1$ and $\hat{\mathbf{b}}_2$ have not been explicitly defined, as it was not required in defining the inertia of the single bar, due to it's symmetry. These directions are most conveniently defined in terms of the node positions that terminate the ends of the bar. To achieve this, the unit vector $\hat{\mathbf{b}}_2$ is defined by the normal vector to the plane created by the vectors $\mathbf{n}_i$ and $\mathbf{n}_j$. Then, vector multiply $\hat{\mathbf{b}}_2$ with $\hat{\mathbf{b}}_3$ to determine $\hat{\mathbf{b}}_1$.

In summary

$$ {}^{k}[\hat{\mathbf{b}}_3]^e = \frac{{}^{k}\mathbf{n}_j - {}^{k}\mathbf{n}_i}{\|{}^{k}\mathbf{n}_j - {}^{k}\mathbf{n}\|} \tag{3.13} $$

$$ {}^{k}[\hat{\mathbf{b}}_2]^e = \frac{{}^{k}\mathbf{n}_j \times {}^{k}\mathbf{n}_i}{\|{}^{k}\mathbf{n}_j \times {}^{k}\mathbf{n}_i\|} \tag{3.14} $$

$$ {}^{k}[\hat{\mathbf{b}}_1]^e = {}^{k}[\hat{\mathbf{b}}_2]^e \times {}^{k}[\hat{\mathbf{b}}_3]^e \tag{3.15} $$

$$ {}^{k}\mathbf{R} = \left[{}^{k}[\hat{\mathbf{b}}_1]^e \quad {}^{k}[\hat{\mathbf{b}}_2]^e \quad {}^{k}[\hat{\mathbf{b}}_3]^e \right] \tag{3.16} $$

Now the inertia of the k^{th} bar is described in the wheel-fixed frame. Since it is rotating about the center of the wheel, the parallel axis theorem must be employed to compute the inertia matrix of the k^{th} bar about the center of the wheel

$$ [{}^{k}\tilde{\mathbf{I}}_w]^e = [{}^{k}\tilde{\mathbf{I}}_c]^e + m_k \left({}^{k}|\mathbf{r}|^2 \, \mathbb{I} - {}^{k}\mathbf{r} \, {}^{k}\mathbf{r}^T \right) \tag{3.17} $$

Where $\mathbf{r}$ is the position of the center of mass of the rod in the wheel-fixed frame. Finally, the total inertia matrix of the wheel is the sum of the inertia matrix about the center of the wheel of all members. The $(1,1)$ component of the total inertia matrix is I_1 and is of special interest because the wheel is assumed to be rolling in the $\hat{\imath}_2, \hat{\imath}_3$ plane, about the $\hat{\imath}_1$ axis.

$$ [\tilde{\mathbf{I}}_T]^e = \sum_{i=1}^{m} [{}^{i}\tilde{\mathbf{I}}_w]^e \tag{3.18} $$

$$ I_1 = \tilde{\mathbf{I}}_T \, (1,1) \tag{3.19} $$

3.3 Rolling Response of the 3-Bar Tensegrity Wheel

As mentioned previously, the assumptions made in deriving the dynamic equations of tensegrity structures offer a lightweight and versatile method to explore the resultant response of the structure caused by changes of geometric parameters. Of prime interest regarding the 3-bar wheel is what parameters most affect how smooth the wheel rolls, how stable the rolling is, and what

can be done to improve traction? Importantly, the design of this structure offers the ability to manipulate the string lengths, whereby the topology of the structure may be controlled. Given terrain requirements, the proper configuration can be determined and the wheel will morph to meet the challenge. For example, a soft, deep terrain of sand would require a deeper penetrating tread for the wheel to achieve the traction necessary to overcome slip. In response, the wheel's outer tread would narrow, or potentially the outer radius would increase, to increase the bars' angle with the ground and thus the ability for the bars to penetrate into the soft sand. Propelling the wheel forward through actuation of the 3-bar prisms has also been theorized. This could be done by controlling the angle the contact members make with the ground such that the wheel either pushes itself forward, or the center of gravity changes and induces rolling.

3.3.1 Dependencies of Smooth Rolling

How smooth the wheel rolls is most affected by the number of sides of the wheel. Consider a case of motion where the wheel is on a sufficiently firm slope such that the wheel remains at the top of the surface. While the wheel rolls, a discrete period of the rotation can be considered as it rotates about a single node that is in contact with the ground from $\left[\frac{\pi}{n}, -\frac{\pi}{n}\right]$, this is shown using three frames of an $n = 8$ wheel in figure 3.8. The axes of the figure are aligned in the $\hat{\imath}$ frame, which is aligned with the incline, so the wheel appears to be rolling on flat ground.

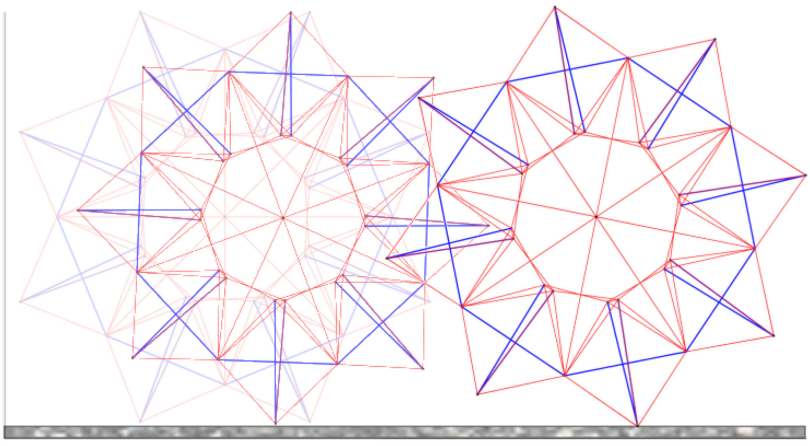

Figure 3.8: 3-Bar Wheel at $t = 0; t = 1.5; t = 3$ seconds

By increasing the number of sides, the gap between the contact nodes is reduced. Therefore, the total angle the wheel travels on, and the maximum value of that angle, during motion of a given set of contact nodes is reduced, see figure 3.9. Also, as the number of sides tends to very high numbers, the wheel itself will tend to a rigid continuum wheel since there are more rigid members for the same overall geometry.

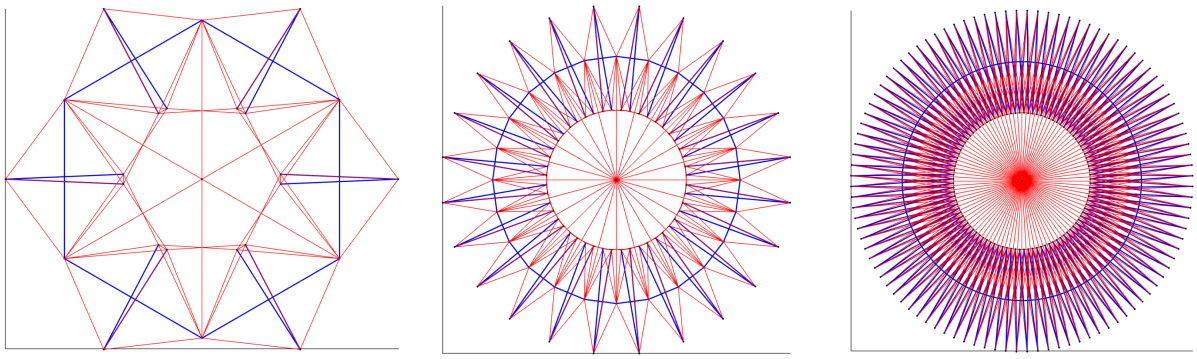

Figure 3.9: 3-Bar Wheels of Complexity (left to right) 6, 24, 100

Upon incidence of the next set of contact nodes, an impulse force is exerted along with the near-instantaneous transfer of weight from the now-uphill nodes and the new downhill node. Dependent on the stiffness and friction of the ground, the impulse the wheel experiences will either cause the wheel to bounce and temporarily lose contact with the ground, or it will begin to roll about the new point. The impulse is a function of the incoming angular velocity of the contact point, and also the angle at which it arrives. Also important is the new in-plane reaction force that is required to keep the new contact point from slipping up or down the hill as it rolls. As the complexity of the 3-bar wheel increases, the impulse experienced by the new contact points is expected to decrease. This is postulated because the direction of the impulse force is opposite to direction of the velocity of the incoming contact node. So, the incoming member belonging to a higher complexity wheel will be arriving to the ground at an angle that is more perpendicular to the slope than that of a lower complexity. Equivalently, this means the velocity vector of the incoming nodes will be

more parallel with the surface at higher complexities. Therefore, the component of the impulse perpendicular to the slope will reduce as the complexity of the wheel increases. This means weight transfer to the new members will be smoother and the wheel will not bounce or shudder as it rolls. To test this postulate, simulations using $n = 8, 12, 16, 24$ wheels on a $50°$ incline were run for a simulation time of 10 seconds. The time history of the axle's deviation from equilibrium point in the $\hat{\imath}_3$ direction are presented in in figure 3.10. Errors in modeling the ground forces result in the entire wheel deviating from what is the "ground", however the oscillations of the axle position are the major focus of these results. Indeed, as the complexity increases the oscillation in the axle position, what would be considered a bumpy ride, decreases.

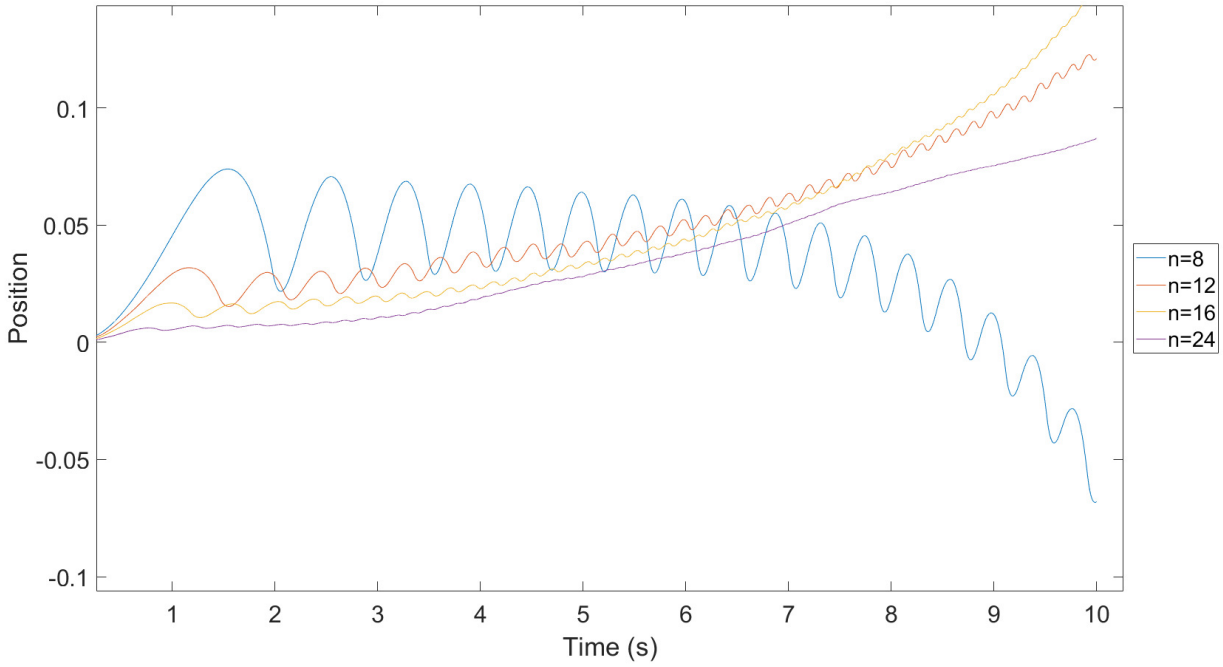

Figure 3.10: Axle $\hat{\imath}_3$ Displacement for $n = 8, 12, 16, 24$, $\varphi = 50°$

The reaction force as a function of time for $n = 8$ and $n = 16$ wheels are shown in figure 3.11. As the wheels reach terminal velocity, there is evidence of the beginnings of steady state force application. The steady state forces of these discrete wheels may be related to the continuum

through some shape factor. The results presented here will form the basis for future work which will attempt to characterize this geometric factor as a function of the complexity. It is expected that the forces will reach to that of the continuum wheel as the complexity reaches infinity.

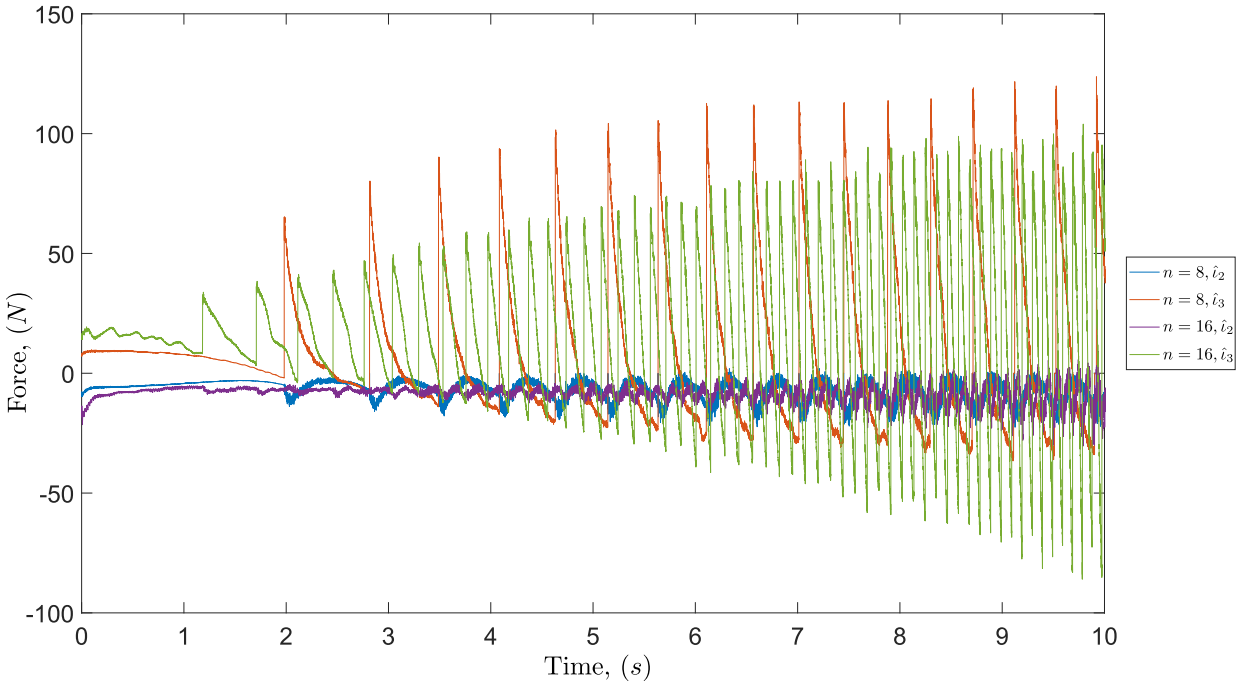

Figure 3.11: Reaction Force History for $n = 8, 16$

3.3.2 Out of Plane Stability

The stability of the wheel in response to out of plane forces is dependent on the outer tread width and outer radius. This is demonstrated by considering an externally applied force to the axle of the wheel in the $-\hat{\mathrm{e}}_1$ direction while the wheel is on flat ground. Assuming the wheel will rotate about the far contact node, if the moment couple of the applied force and the friction with the ground is larger than the couple caused by the normal force and the ground reaction, the wheel will begin to tip. The forces, shown in figure 3.12, are summed to zero to obtain the relation between the weight force and normal force. This also provides an equation for the friction force required for the wheel to not slide across the ground. Then, the moments about point A are evaluated.

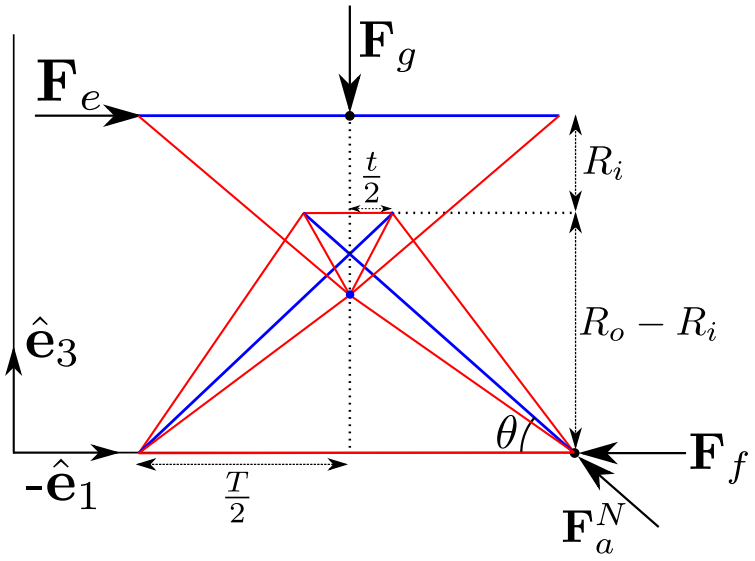

Figure 3.12: Tip-Over Free Body Diagram

$$\sum \mathbf{F} = \mathbf{0} \tag{3.20}$$

$$\hat{\mathbf{e}}_3 : \ 0 = -F_a^N \cos\theta + F_e - F_f \tag{3.21}$$

$$\hat{\mathbf{e}}_1 : \ 0 = F_a^N \sin\theta - F_g \rightarrow F_a^N = \frac{mg}{\sin\theta} \tag{3.22}$$

$$F_f = F_e - mg\cot\theta \tag{3.23}$$

$$\sum \mathbf{M}_a = \left(-F_e R_0 + F_g \frac{T}{2}\right) \hat{\mathbf{e}}_2 \tag{3.24}$$

$$tip\ when\ F_e > \frac{mg}{2}\frac{T}{R_0} \tag{3.25}$$

$$F_e > \frac{mg}{2}\rho; \qquad \rho = \frac{T}{R_0} \tag{3.26}$$

Thus, to make the wheel more resistant to tipping, the value of ρ must be increased which is done by increasing T or decreasing R_0. According to the wheel's geometry,

$$\tan\theta = \frac{\frac{1}{2}(T+t)}{R_0 - R_i} = \rho\frac{1+\varepsilon}{1-\sigma}; \quad \varepsilon = \frac{t}{T};\ \sigma = \frac{R_i}{R_0} \tag{3.27}$$

Physically, R_i is contained within R_o thus $0 < \sigma < 1$, and $\varepsilon > 0$. Given ρ, the expression for the friction force at the critical tipping point where the inequality 3.25 becomes an equation is

$$F_f = F_e - \rho \frac{mg}{2} \frac{1+\varepsilon}{1-\sigma} = F_e \left(1 - \frac{1+\varepsilon}{1-\sigma}\right) \tag{3.28}$$

$$F_f' = \frac{F_f}{F_e} = 1 - \frac{1+\varepsilon}{1-\sigma} \tag{3.29}$$

Equation 3.29 provides what the friction force, normalized by the external load, would need to be for the wheel to not slip as it tips. The normalized friction as a function of σ and ε is shown in figure 3.13 below.

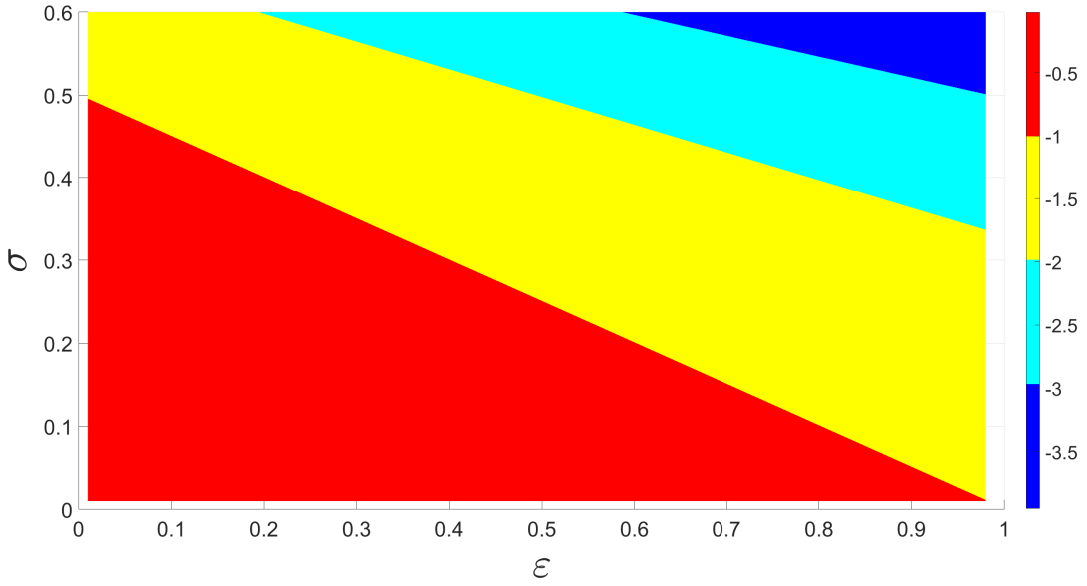

Figure 3.13: Normalized Friction as a function of σ and ε

The region in red is the region that the friction force is a fraction of the external load, which is preferable. The values seen on the scale are negative since the friction force is resisting the external force, which is positive. The magnitude of forces in the bottom left corner of the map are the minimum since angle theta decreases as both σ and ε increase, reducing the contribution

of the force normal to the ground and increasing the demand of the friction force. As previously mentioned, a smaller angle with the ground resists tipping, so there is an inverse relation with the angle to the ground between slipping and tipping that must be balanced according to the ground's friction. If the ground's coefficient of static friction is insufficient to supply this kind of force, the wheel will slide as it tips over.

3.3.3 Limitations of the 3-Bar Wheel

It is important to note current limitations observed in this wheel. Mainly, the 3-bar prism is not an ideal structure to withstand the bending forces that are applied due to the perpendicular friction forces. Tensegrity structures are most efficient when members are placed along the direction of forces, so when the bars are perpendicular to the friction, it is not efficient. Acknowledging this, investigation into tensegrity structures that are optimal in bending was conducted to determine if there was a more suitable prism available that could still model this approach. The following chapters will introduce tensegrity structures ideal for bending loads and a new truss that extends beyond planar bending in an effort to support off-nominal loads out of the plane.

3.4 Concluding Remarks

The main contribution of this chapter is the introduction of a new toroidal tensegrity topology. The motivation for the development, and further analysis, of this topology is to advance the science of toroidal tensegrity structures, which has grown at a slower pace compared to its geometric counterparts. Further, toroidal structures previously published are designed for dome applications. In contrast, application of this structure is in the locomotion system of small space rovers or other lightweight vehicles. Indeed, beyond the clichés and quips, this chapter asserts that humanity's oldest invention can still be improved.

4. TENSEGRITY STRUCTURES IN BENDING

An optimal geometry to support bending loads was first proposed by Michell [59]. Discrepencies and improvments to the optimality conditions have been identified and published by Rozvany [60]. Skelton pushed Michell's theory into the paradigm of tensegrity by forming a discrete model of Michell's original truss [1], which matches Michell's work as the complexity reaches inifinity. The following is a summary of Skelton's work, which introduces the parameters that describe 2D Michell truss and forms the foundation for the new truss, the 3D Michell truss, that extends this design into the third dimension. This new topology answers the question of how can an optimal bending truss in the plane be designed to support out-of-plane forces? Analysis of the equilibrium of this new truss, given a range of external bending force direction, results in regions of nominal operation for a complexity 1 truss. This result is generalized to any complexity by introducing additional strings that limit the variation of member force direction such that the region of operation for a general complexity is equivalent to complexity 1.

4.1 2D Michell Truss

The Michell spiral is defined using the parameters q, r_0, β and ϕ. β and ϕ define the departure angle of each member and the segmentation angle of the base circle, respectively. The parameter r_0 is the length from the center of the base circle to the tip node, typically called the *initial radius*. Finally, q defines the *complexity* of the Michell spiral which governs the number of end to end connections that are made. See figure 4.1 for a visual representation.

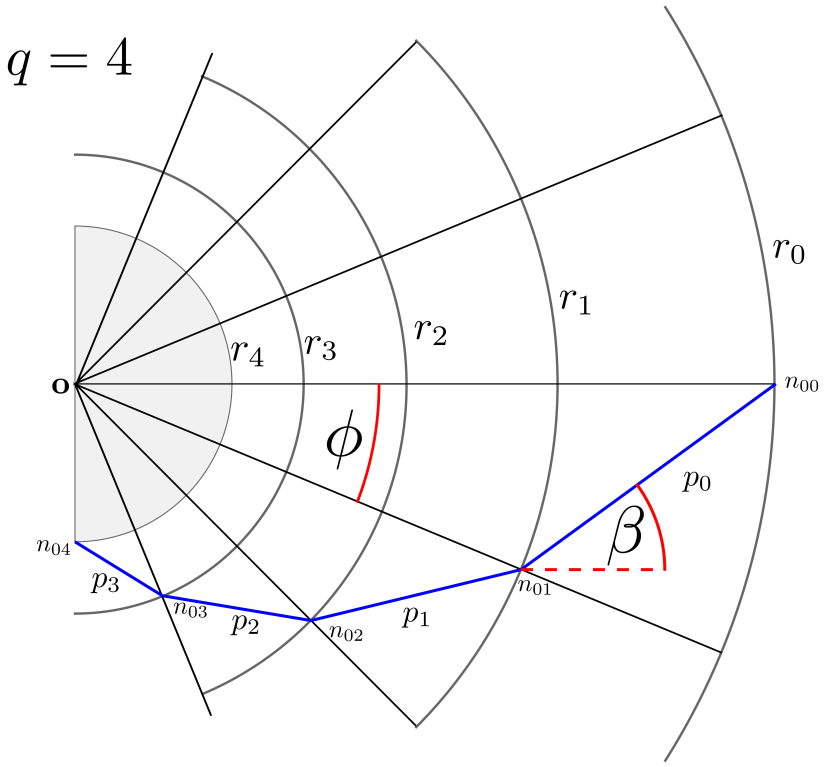

Figure 4.1: Michell Spiral of Complexity 4, $\phi = \frac{\pi}{8}$, $\beta = \frac{\pi}{6}$, [1]

The subsequent radii and member lengths, p_i are defined using a recursive formula

$$r_{i+1} = ar_i, \quad p_i = cr_i, \quad i = 0, 1, 2, ..., q \tag{4.1}$$

$$a = \frac{\sin(\beta)}{\sin(\beta + \phi)} \tag{4.2}$$

$$c = \frac{\sin(\phi)}{\sin(\beta + \phi)} \tag{4.3}$$

Now, consider the nodes of a set of Michell spirals from complexity 4 to 0 (see figure 4.2) such that the spiral of order 4 consists of the connections between nodes $\mathbf{n}_{00}, \mathbf{n}_{01}, \mathbf{n}_{02}, \mathbf{n}_{03}, \mathbf{n}_{04}$. The spiral of order 3 connects nodes $\mathbf{n}_{10}, \mathbf{n}_{11}, \mathbf{n}_{12}, \mathbf{n}_{13}$. The spiral of order 2 connects $\mathbf{n}_{20}, \mathbf{n}_{21}, \mathbf{n}_{22}$. The spiral of order 1 connects the pair $\mathbf{n}_{30}, \mathbf{n}_{31}$; and finally order 0 is node $\mathbf{n}_{40}$. This notation remains consistent for the assigned complexity of the Michell topology.

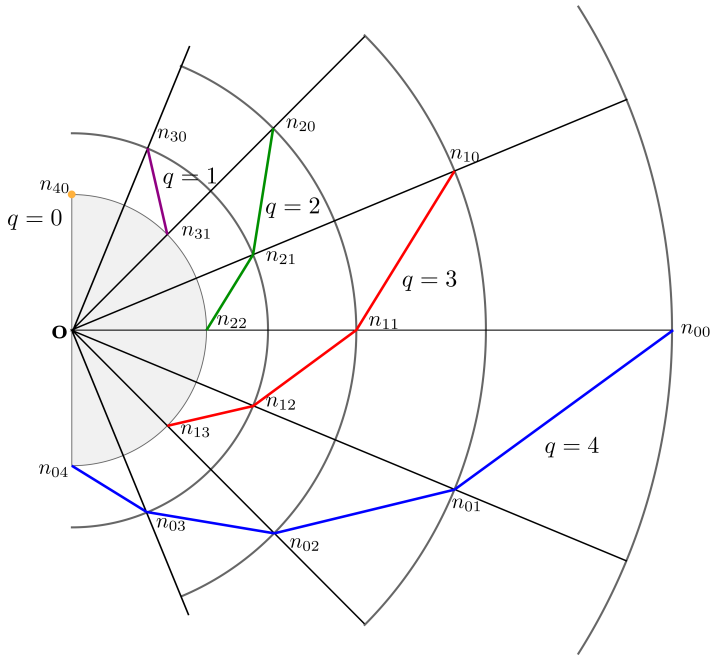

Figure 4.2: Michell Spiral of Complexity 0,1,2,3, and 4, $\phi = \frac{\pi}{8}$, $\beta = \frac{\pi}{6}$

Two important geometric equalities to note:

1. Relative to the common origin, **0**, nodes lying on the same radius have the same magnitude

$$\|\mathbf{n}_{ik}\| = \|\mathbf{n}_{mn}\| \; for \; all \; i + k = m + n \tag{4.4}$$

2. Nodes along the same radial band are related by a phase shift of $2m\phi$

$$\mathbf{n}_{i+m,k-m} = e^{j2m\phi}\mathbf{n}_{ik} \tag{4.5}$$

Where m is an integer and $e^{j2m\phi}$ describes vectors in the complex plane. Members of the spiral are defined by the vector connecting nodes $\mathbf{n}_{ik}$ and $\mathbf{n}_{i,k+1}$ such that

$$\mathbf{m}_{ik} = \mathbf{n}_{ik} - \mathbf{n}_{i,k+1} \tag{4.6}$$

$$\mathbf{n}_{ik} = n_{ik}e^{j\varphi_{n_{ik}}}, \quad n_{ik} = r_{i+k}, \quad \varphi = (i-k)\phi \tag{4.7}$$

Where n_{ik} and $\varphi_{n_{ik}}$ are the magnitude and phase of the vector $\mathbf{n}_{ik}$ respectively; and r_k satisfies equation 4.1 for some specified r_0. According to these definitions, it is clear that members within the same radius band are of equal length. The mirror image of all members reflected about the axis $(\mathbf{0}, \mathbf{n}_{00})$ define the conjugates of the vectors $\mathbf{m}_{ik,}$ such that

$$\overline{\mathbf{m}}_{ik} = \overline{\mathbf{n}_{ik} - \mathbf{n}_{i,k+1}} = \mathbf{n}_{ki} - \mathbf{n}_{k+1,i} \tag{4.8}$$

The collection of $\mathbf{m}_{ik}$ and their conjugates forms the Michell topology shown in figure 4.3 below.

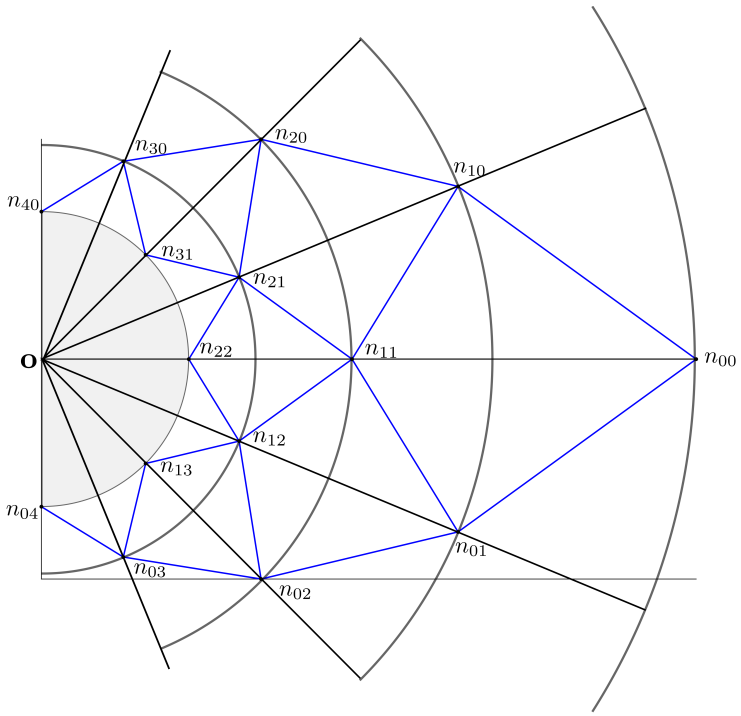

Figure 4.3: Michell Topology of Complexity 4, $\phi = \frac{\pi}{8}$, $\beta = \frac{\pi}{6}$

Starting at the tip node, a recursive method of joints is performed to calculate the direction of member forces. Within two regions of bending direction, θ_{00}, a tensegrity truss may be constructed. These regions, shown in figure 4.4, denote when the global truss is in pure bending. Given a

bending load in the blue region, $(\pi + \beta \leq \theta_{00} \leq 2\pi - \beta)$, each blue member is in compression and each red member is in tension. Conversely, the red region, $(\beta \leq \theta_{00} \leq \pi - \beta)$, denotes that the red members are in compression and blue members are in tension.

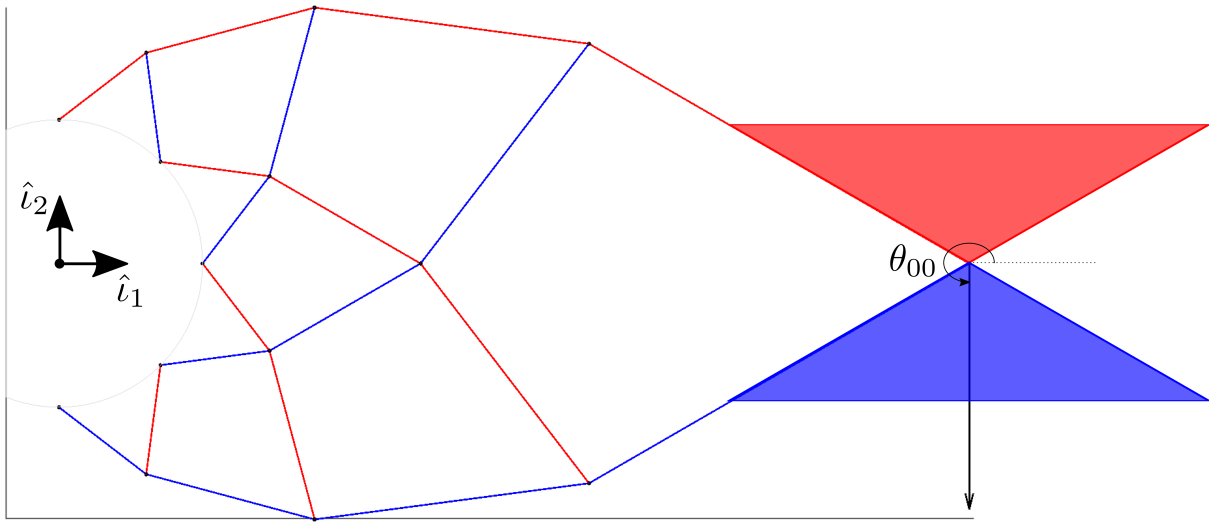

Figure 4.4: Michell Topology of Complexity 4, Force Regions of Interest

Given that the member forces are determined *a priori*, Skelton derives analytical solutions for the minimum mass of this truss, and optimal angles for $\phi,\ \beta$. Optimal complexity, q, is also derived when assuming a penalty for joint mass. Using those derivations, it is proven that the discrete Michell truss is the optimal-mass solution to support a single bending load at the tip. The objective of this present work is to form a spatial truss using the parameters of this planar truss. Then, the triangular region of interest is transformed into a conic section and provides a working envelope of out-of-plane bending force, given a chosen design.

4.2 3D Michell Topology Introduction

Out of plane forces are not supported by the two dimensional Michell structure detailed in Section 4.1. Therefore, there is a question of how can the planar truss be re-designed to support off-nominal loads out of the plane? Such a design may be a sub-optimal, but still low-mass, solution that exhibits improved support against out-of-plane forces. This chapter introduces a new topology, the 3D Michell truss, which serves as a solution to this question. By using the planar truss as the basis for the new topology, a mass penalty can be quantified to understand the cost tomass optimality the spatial truss incurs.

The circular base geometry of the 2D Michell transforms into a cylinder for this new topology by introducing a parameter to define the out of plane displacement from the origin. This distance is considered using two different coordinate methods: one using cylindrical coordinates about the origin and another using spherical coordinates. All other required parameters are derived from the 2D Michell topology in figure 4.1. Most notably, the parameter β is used to determine the radii of each complexities' cylinder. Then, that radius is subsequently used for the node positions. The two-index method of describing the general node position is replaced by a four index method. An iterative pattern for locating the nodes beyond the principal node at the tip is detailed, and examples of node locations are provided for both coordinate representations.

The following section will discuss the indexing method in full. Then, the out-of-plane parameter for spherical and cylindrical coordinates is defined. The subsequent section will provide an analytical appraoch to the force propagation for a general structure, with examples for complexity 1 trusses. The final two sections provide computation of the minimal material volume given specific material choices, and an investigation in the effect of adding additional strings to stiffen the truss.

4.3 3D Michell Parameters

4.3.1 Node Indexing

The two-index method, n_{ik}, of the planar truss is replaced by a four-index method, n_{UDLR}. The index values (U, D, L, R) describe the relative position of a node to the principal node, $\mathbf{n}_{0000} = [0\ r_0\ 0]^T$. According to a node's index, the integer values $\mathbb{X} = L - R$ and $\mathbb{Z} = U - D$ are computed and used as inputs to a general equation describing the location of a node, given the choice of spherical or cylindrical coordinates. The node locations of a complexity q 3D Michell topology are determined by following an iterative pattern until the entire topology is generated. Complexity $q = 0$ is simply the principal node extended from the origin by r_0 along the $\hat{\imath}_2$ axis. The next complexity of the topology, and indeed each subsequent complexity, is realized by creating three 'offspring' nodes from each node in the current complexity. The indices of the three nodes are updated, respectively, by

1. U+1; L+1

2. U+1; R+1

3. D+1

Following this rule, the total number of nodes, n_k, for a given complexity set, k is defined by

$$n_k = \frac{k\,(k+1)}{2} \tag{4.9}$$

Therefore, the total number of nodes, n, for a given complexity truss, q, is

$$n = \sum_{k=1}^{q+1} n_k = \sum_{k=1}^{q+1} \frac{k\,(k+1)}{2} \tag{4.10}$$

4.3.2 Cylindrical Coordinate Parameterization - δ

Consider the circular origin of the 2D Michell topology and its subsequent extension out of the plane to form a base cylinder. The parameter, δ, is a distance that defines how far along the $\hat{\imath}_1$ axis

a node is from the origin. Under this parameterization, the general position of a node is

$$\mathbf{n}_{UDLR} = r_q \begin{bmatrix} \mathbb{X}\delta \\ \cos\left(\mathbb{Z}\phi\right) \\ \sin\left(\mathbb{Z}\phi\right) \end{bmatrix} \tag{4.11}$$

The distance from the center does not grow linearly as complexity increases because the node positions are multiplied by the radius of the current complexity and the integer value $\mathbb{X}$. A 3D topology of complexity q is created by following the iterative method presented in the previous section. As an example, the node positions for a complexity one $(q = 1)$ structure is

$$\mathbf{n}_{1010} = r_1 \begin{bmatrix} \delta \\ \cos\left(\phi\right) \\ \sin\left(\phi\right) \end{bmatrix} \quad \mathbf{n}_{1001} = r_1 \begin{bmatrix} -\delta \\ \cos\left(\phi\right) \\ \sin\left(\phi\right) \end{bmatrix} \quad \mathbf{n}_{0100} = r_1 \begin{bmatrix} 0 \\ \cos\left(-\phi\right) \\ \sin\left(-\phi\right) \end{bmatrix}$$

A topology of complexity 2 would then apply the rule to the three nodes listed above. A topology of complexity 3 is produced, again, by the rules applied to the six nodes created in complexity 2, and so on up to complexity q. A top-down sketch of a complexity 3 truss is shown in figure 4.5 to visualize the parameter δ and how it influences the out-of-plane distance given q and $\mathbb{X}$.

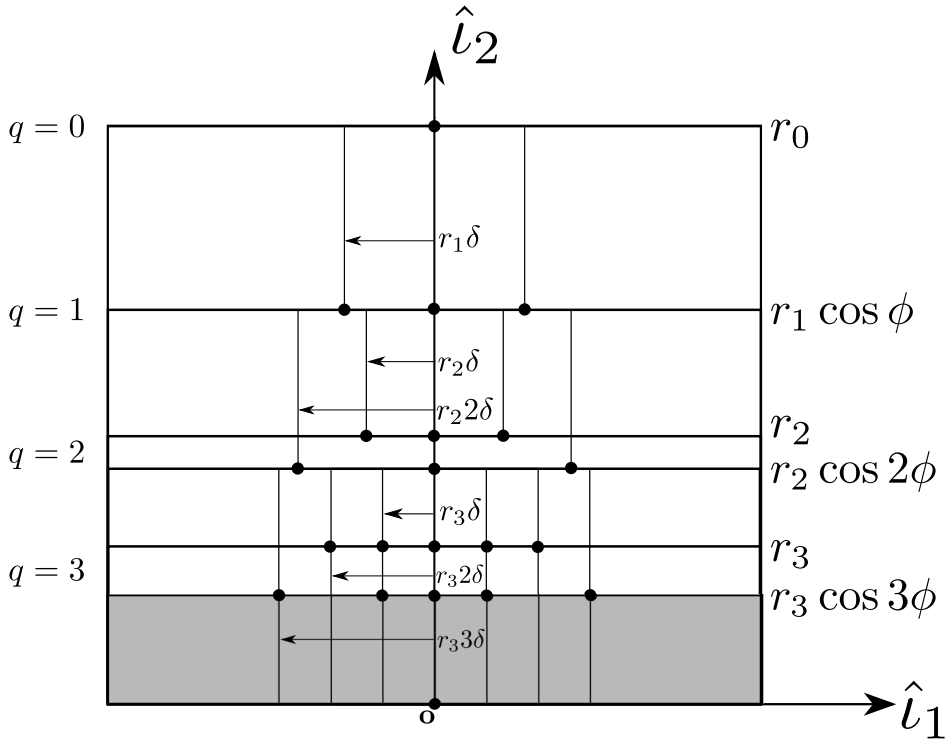

Figure 4.5: Sketch of δ Parameter

A 3D Michell truss of complexity 4 is shown below. Notice in figure 4.6, the projection of the truss on the $\hat{\imath}_2, \hat{\imath}_3$ plane is precisely the 2D Michell truss.

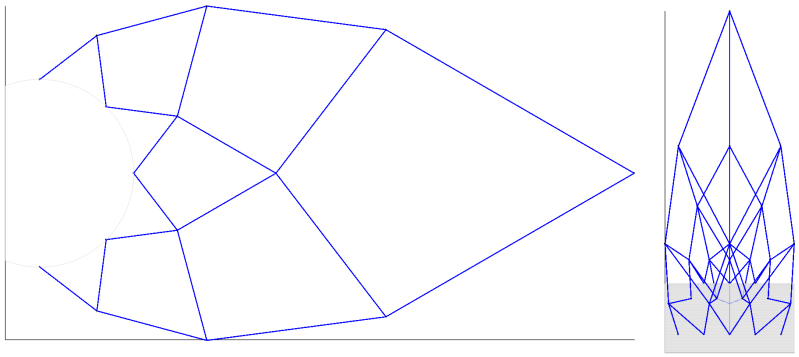

Figure 4.6: 3D Michell Topology of Complexity 4 - Side and Top View, $\phi = \frac{\pi}{8}$, $\beta = \frac{\pi}{6}$, $\delta = \frac{r_0}{4}$

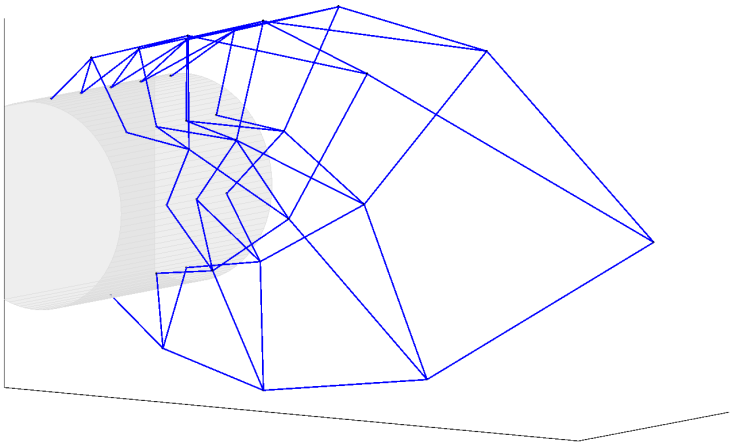

Figure 4.7: 3D Michell Truss of Complexity 4 - Isometric View, $\beta = \frac{\pi}{6}$, $\delta = \frac{r_0}{4}$

4.3.3 Spherical Coordinate Parameterization - ε

The parameter ε is defined as a segmentation angle from the origin, shown in figure 4.8, in the $\hat{\iota}_1, \hat{\iota}_2$ plane. The distance away from the origin along $\hat{\iota}_1$ is prescribed by constraining the projection of nodes on the $\hat{\iota}_1, \hat{\iota}_2$ plane to coincide with the rays eminating from the origin.

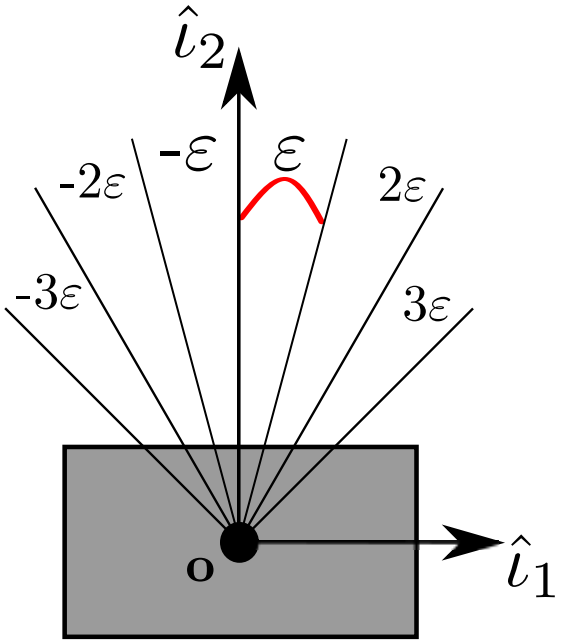

Figure 4.8: Sketch of Segmentation Angle, ε

Thus, given the parameter ε and the integer values $\mathbb{X}, \mathbb{Z}$, the general location of a node with indices (U, D, L, R) is calculated by

$$\mathbf{n}_{UDLR} = r_q \begin{bmatrix} \cos(\mathbb{Z}\phi)\tan(\mathbb{X}\varepsilon) \\ \cos(\mathbb{Z}\phi) \\ \sin(\mathbb{Z}\phi) \end{bmatrix} \tag{4.12}$$

The same iterative method for updating node indices is followed. For a complexity 1 truss using spherical coordinates, the locations of the nodes are

$$\mathbf{n}_{1010} = r_1 \begin{bmatrix} \cos(\phi)\tan(\varepsilon) \\ \cos(\phi) \\ \sin(\phi) \end{bmatrix} \quad \mathbf{n}_{1001} = r_1 \begin{bmatrix} \cos(\phi)\tan(-\varepsilon) \\ \cos(\phi) \\ \sin(\phi) \end{bmatrix} \quad \mathbf{n}_{0100} = r_1 \begin{bmatrix} 0 \\ \cos(-\phi) \\ \sin(-\phi) \end{bmatrix}$$

To provide a detailed view of the 3D Michell with spherical coordinates, an example of top-down and isometric views of an complexity 2 topology is shown in figures 4.9 and 4.10 below. The different colors of the left image in figure 4.9 correspond to the $\mathbb{Z}$ value which governs the height above or below the $\hat{\imath}_1, \hat{\imath}_2$ plane.

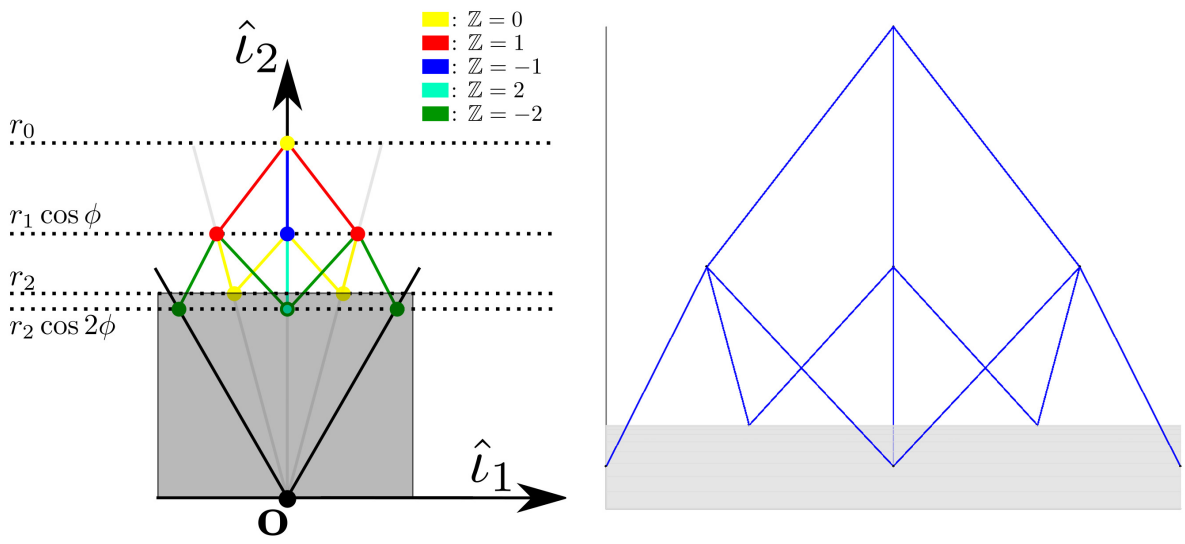

Figure 4.9: XY View of 3D Michell Topology of Complexity 2; $\beta = \frac{\pi}{6},\ \phi = \frac{\pi}{16};\ \varepsilon = \frac{\pi}{12}$

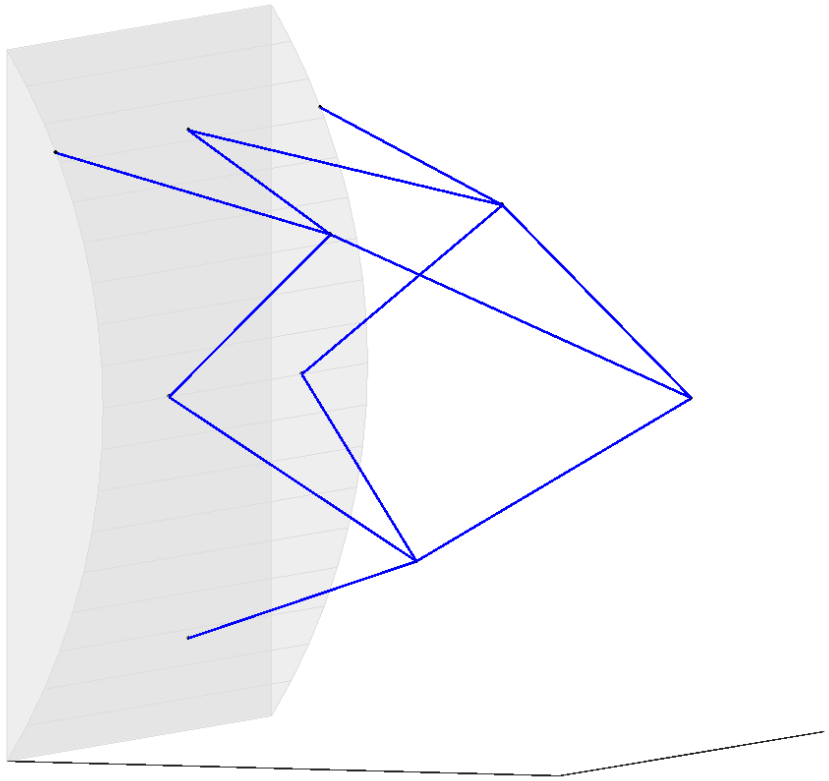

Figure 4.10: 3D Michell Truss of Complexity 2; $\beta = \frac{\pi}{6},\ \phi = \frac{\pi}{16};\ \varepsilon = \frac{\pi}{12}$

A 3D Michell truss of complexity 4 using the spherical coordinates is shown below to compare with the cylindrical coordinate truss. The major difference for these two trusses is how the nodes at the final complexity are grouped, and also the distribution of nodes out of the plane. Notice, again, that the spherical coordinate truss also is exactly the 2D truss in the YZ plane. It is important to note that because the tangent is involved, ε and q must be chosen such that singularities at or near $\frac{-\pi}{2}$ and $\frac{\pi}{2}$ are avoided, specifically, $0 \geq |q\varepsilon| < \frac{\pi}{2}$.

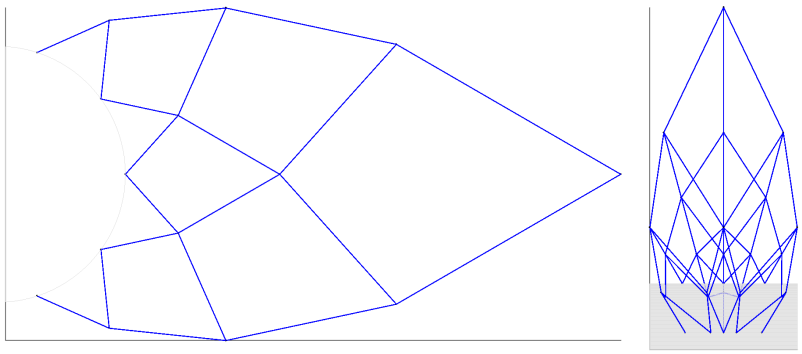

Figure 4.11: 3D Michell Truss of Complexity 4 - YZ and XY View; $\beta = \frac{\pi}{6},\ \phi = \frac{\pi}{10};\ \varepsilon = \frac{\pi}{12}$

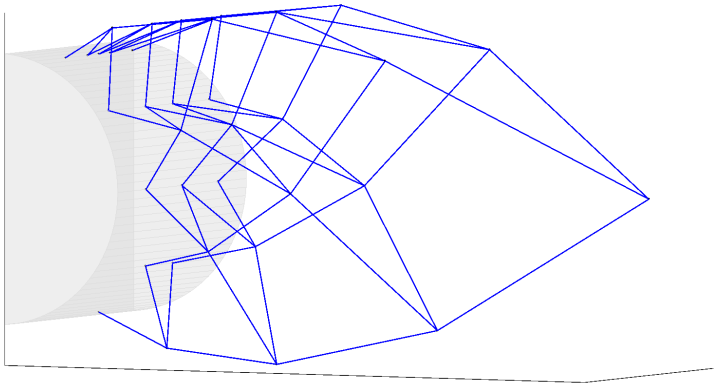

Figure 4.12: 3D Michell Truss of Complexity 4; $\beta = \frac{\pi}{6},\ \phi = \frac{\pi}{10};\ \varepsilon = \frac{\pi}{12}$

4.4 3D Michell Force Propagation

Tensegrity structures boast the property that members are uni-axially loaded. Additionally, members are designed to be sufficiently stiff such that external forces do not cause rigid body deformations. Given these two facts, the direction of force of each member in the 3D truss can be calculated using a recursive method of joints. Assuming a single bending load at the tip, this recursive method begins with equilibrium at the principal node to compute the forces of the complexity 1 members. Acording to the sign of the force, the type of member (cable or bar) may be determined *a priori* and is valid for a given nominal region of external force directions. This method will first be presented for a complexity 1 truss using cylindrical and spherical coordinates as an example. Then, the forces at a general node is formulated to create the basis for the recursive methods valid for a general complexity.

4.4.1 Example: Complexity 1 Forces Using Cylindrical Coordinates

Consider a complexity $q = 1$ 3D Michell truss with parameters r_0, β, ϕ, δ, and an applied force at the tip, $\mathbf{w}_0$, with azimuth and declination φ, γ, respectively, such that

$$\mathbf{w}_0 = w_0 \begin{bmatrix} \cos\varphi \sin\gamma \\ \sin\varphi \sin\gamma \\ \cos\gamma \end{bmatrix} \tag{4.13}$$

Equilibrium is maintained when

$$\sum \mathbf{F} = \lambda_{1010}\mathbf{m}_{1010} + \lambda_{1001}\mathbf{m}_{1001} + \lambda_{0100}\mathbf{m}_{0100} - \mathbf{w}_0 = \mathbf{0} \tag{4.14}$$

In reference to figure 4.13, the member from n_{1010} to node n_{0000} corresponds to the vector $\mathbf{m}_{1010}$. The connection from nodes n_{1001} to n_{0000} and n_{0100} to n_{0000} are vectors $\mathbf{m}_{1001}$ and $\mathbf{m}_{0100}$, respectively. $\lambda_{1010}, \lambda_{1001}, \lambda_{0100}$ are the force densities of each of these members. Solving this equation for $\lambda_{1010}, \lambda_{1001}, \lambda_{0100}$ yields

$$\lambda_{1010} = \frac{w_0}{2r_0\delta ac\sin(2\beta)}\left[(\sin\varphi\sin\gamma\sin\beta - \cos\gamma\cos\beta)\,a\delta - c\cos\varphi\sin\gamma\sin 2\beta\right] \tag{4.15}$$

$$\lambda_{1001} = \frac{w_0}{2r_0\delta ac\sin(2\beta)}\left[(\sin\varphi\sin\gamma\sin\beta - \cos\gamma\cos\beta)\,a\delta + c\cos\varphi\sin\gamma\sin 2\beta\right] \tag{4.16}$$

$$\lambda_{0100} = \frac{w_0}{r_0 c\sin(2\beta)}\left[\sin\varphi\sin\gamma\sin\beta + \cos\gamma\cos\beta\right] \tag{4.17}$$

Consider a special case when the bending force is directly in the $-\hat{\imath}_2$ direction (see figure 4.13), thus $\varphi = 0$ and $\gamma = \pi$. Then, the force density of each member is

$$\lambda_{1010} = \frac{w_0}{4r_0 c\sin\beta} \tag{4.18}$$

$$\lambda_{1001} = \frac{w_0}{4r_0 c\sin\beta} \tag{4.19}$$

$$\lambda_{0100} = -\frac{w_0}{2r_0 c\sin\beta} \tag{4.20}$$

The negative sign in equation 4.20 denotes this member is in compression, therefore it is assigned as a bar (blue). The other two members are in tension and consequently are cables (red).

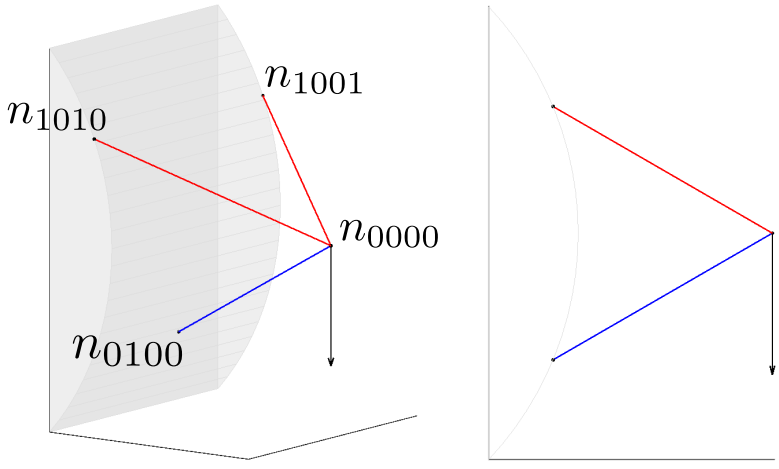

Figure 4.13: 3D Truss, $q = 1$, Red = Tension, Blue = Compression

By rearranging equations 4.15, 4.16, 4.17, the force density of each member is positive (i.e. the member is in tension) if the following inequalities are true,

$$\lambda_{1010} > 0 \; if \;\; (\sin\varphi \sin\gamma \sin\beta - \cos\gamma \cos\beta)\, a\delta > c \cos\varphi \sin\gamma \sin(2\beta) \tag{4.21}$$

$$\lambda_{1001} > 0 \; if \;\; (\sin\varphi \sin\gamma \sin\beta - \cos\gamma \cos\beta)\, a\delta > -(c \cos\varphi \sin\gamma \sin(2\beta)) \tag{4.22}$$

$$\lambda_{0100} > 0 \; if \;\; \sin\varphi \sin\gamma\beta > -(\cos\gamma \cos\beta) \tag{4.23}$$

The results of evaluating these inequalities for a sweep of φ and γ through $[0, 2\pi]$ provides a map of the sign of each member as a function of the direction of the external force load; this is shown in figures 4.14, 4.15, and 4.16 below. For each, blue corresponds to a negative force density leading to the member experiencing compression while the red corresponds to a positive force density and the member is in tension.

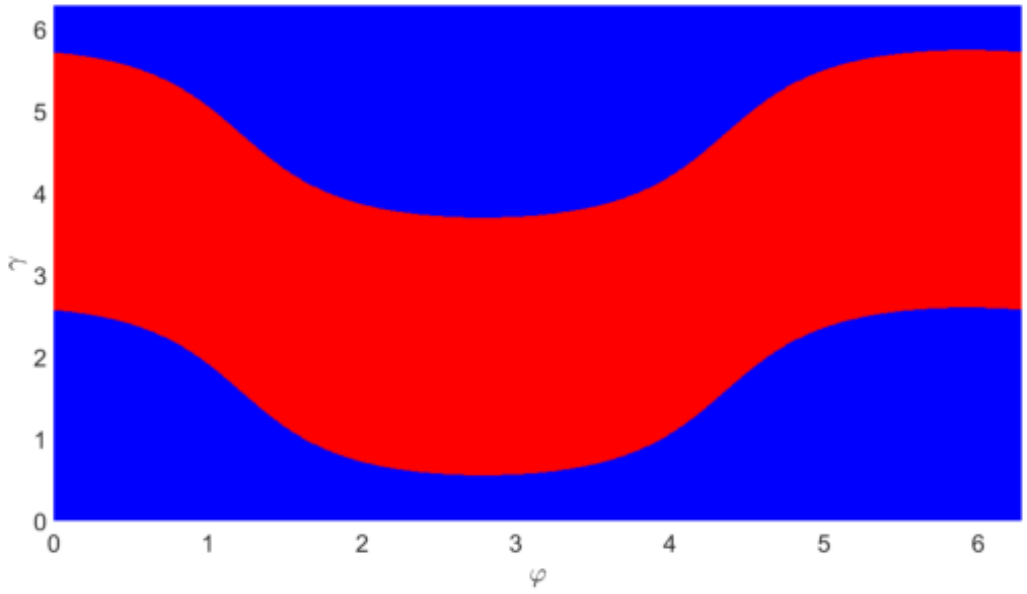

Figure 4.14: Sign of λ_{1010} as a Function of φ, γ (Blue = Compression, Red = Tension)

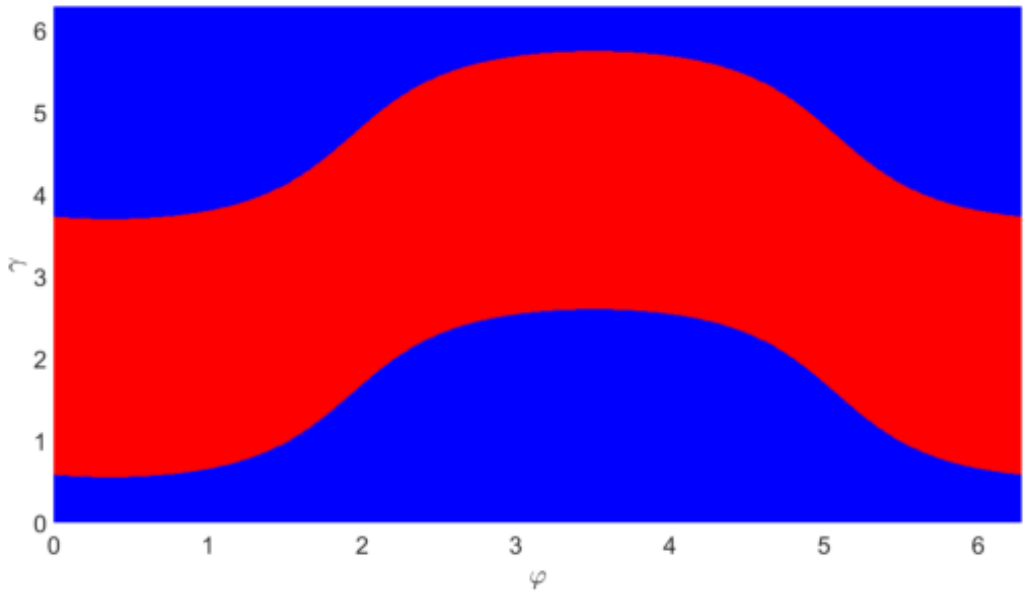

Figure 4.15: Sign of λ_{1001} as a Function of φ, γ (Blue = Compression, Red = Tension)

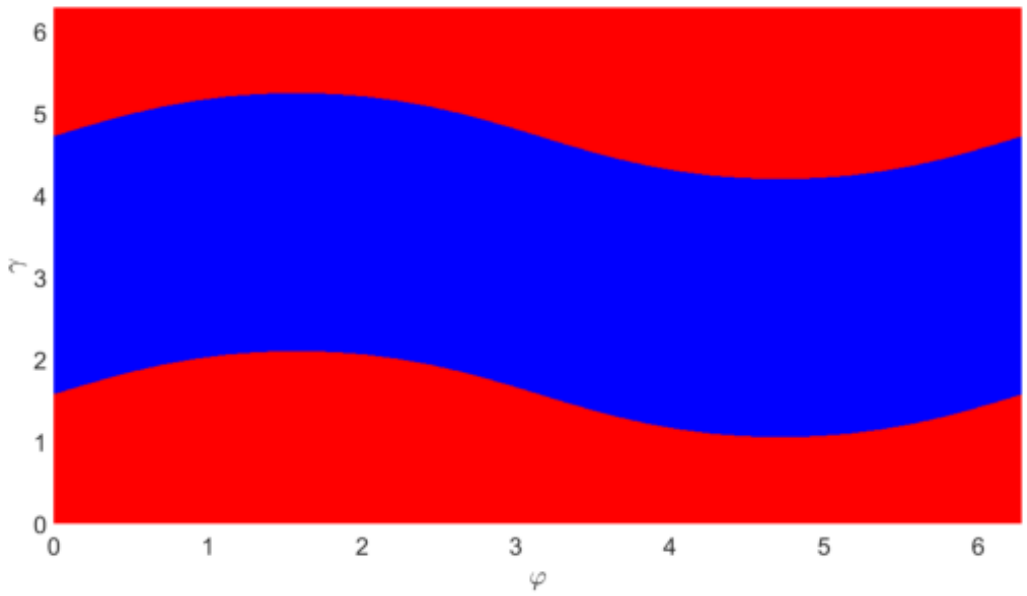

Figure 4.16: Sign of λ_{0100} as a Function of φ, γ (Blue = Compression, Red = Tension)

4.4.2 Example: Complexity 1 Forces Using Spherical Coordinates

Given a complexity $q = 1$ 3D Michell truss with parameters $r_0, \beta, \phi, \varepsilon$, and an applied force at the tip, $\mathbf{w}_0$, equilibrium is maintained when

$$\sum \mathbf{F} = \lambda_{1010}\mathbf{m}_{1010} + \lambda_{1001}\mathbf{m}_{1001} + \lambda_{0100}\mathbf{m}_{0100} - \mathbf{w}_0 = \mathbf{0} \tag{4.24}$$

Solving this equation for $\lambda_{1010}, \lambda_{1001}, \lambda_{0100}$ yields

$$\lambda_{1010} = \frac{w_0}{4}\left[\rho - 2\sigma - \frac{\cos\gamma}{ar_0\sin\phi}\right] \tag{4.25}$$

$$\lambda_{1001} = \frac{w_0}{4}\left[\rho + 2\sigma - \frac{\cos\gamma}{ar_0\sin\phi}\right] \tag{4.26}$$

$$\lambda_{0100} = \frac{w_0}{2}\left[\rho + \frac{\cos\gamma}{ar_0\sin\phi}\right] \tag{4.27}$$

$$\sigma = \frac{\cos\varphi\sin\gamma}{ar_0\cos\phi\tan\varepsilon} \qquad \rho = \frac{\sin\varphi\sin\gamma}{r_0\left(1 - a\cos\phi\right)} \tag{4.28}$$

Consider, again, the case of a single bending load applied downward on the tip node of this structure, $\varphi = 0$ and $\gamma = \pi$. Then the force densities of each member is

$$\lambda_{1010} = \frac{w_0}{4ar_0 sin\phi} = \frac{w_0}{4r_0 c\sin\beta} \tag{4.29}$$

$$\lambda_{1001} = \frac{w_0}{4ar_0 sin\phi} = \frac{w_0}{4r_0 c\sin\beta} \tag{4.30}$$

$$\lambda_{0100} = -\frac{w_0}{2ar_0 sin\phi} = -\frac{w_0}{2r_0 c\sin\beta} \tag{4.31}$$

Due to the symmetry of the truss, the result of this special case is the same regardless of parameterization method and is only dependent on parameters original to the planar truss. Now, forces at a general node will be presented to develop a recursive algorithm that determines the member force directions for any complexity truss.

4.4.3 Forces at a General Node

It is prudent to start the general force computation by establishing the force equilibrium at a single node, given the recursive method of building this truss that was discussed in section 4.3.1. At a given node, n_{UDLR}, it is expected to have up to 3 members going *into* the node, up to 3 members coming *out of* the node and an external force, $\mathbf{w}_{UDLR}$. Here, the phrase *into* means traveling from the numerically higher complexity to the lower complexity. In other words, this direction is defined as going towards the principal node. The phrase *out of* the node describes the members that are of the set of the complexity's current members and connected to nodes of the complexity below. Their direction also moving *towards* the principal node. A sketch of of this description is provided below. It is important to note that the scope of this work considers only the case of a single bending load at the tip. As such, $\mathbf{w}_{UDLR}$ for any $(U, D, L, R) \neq 0$ is null.

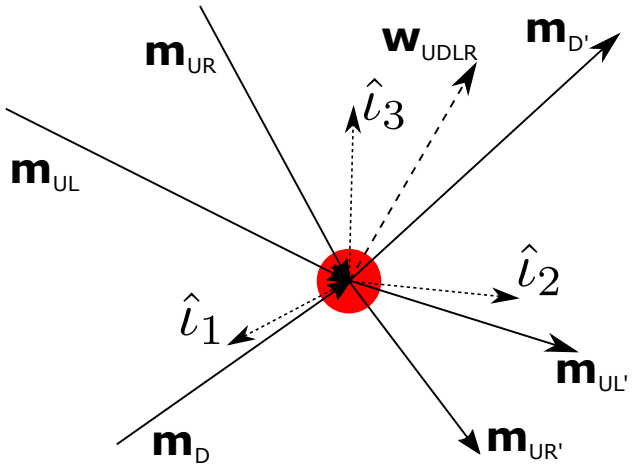

Figure 4.17: n_{UDLR} Internal and External Forces

The sum of all forces going into and out of the given node n_{UDLR} is then given by

$$f_{UL}\frac{\mathbf{m}_{UL}}{\|\mathbf{m}_{UL}\|} + f_{UR}\frac{\mathbf{m}_{UR}}{\|\mathbf{m}_{UR}\|} + f_{D}\frac{\mathbf{m}_{D}}{\|\mathbf{m}_{D}\|} - f_{UL'}\frac{\mathbf{m}_{UL'}}{\|\mathbf{m}_{UL'}\|} - f_{UR'}\frac{\mathbf{m}_{UR'}}{\|\mathbf{m}_{UR'}\|} - f_{D'}\frac{\mathbf{m}_{D'}}{\|\mathbf{m}_{D'}\|} - \mathbf{w}_{UDLR} = 0 \quad (4.32)$$

The vector $\mathbf{m}$ is defined as the difference between two nodes. The un-primed terms belong to the members that are going into the node. The subscript UL defines the member that is coming from the node whose index is $n_{(U+1)D(L+1)R}$, subscript UR corresponds to $n_{(U+1)DL(R+1)}$ and subscript D matches with $n_{U(D+1)LR}$. The primed terms are for the members coming out of the node. These terms have similar subscripts but now the operation is to subtract from that index to denote that it is going to the complexity below the current one. Explicitly, subscript UL' matches node $n_{(U-1)D(L-1)R}$, subscript UR' matches $n_{(U-1)DL(R-1)}$ and subscript D' matches $n_{U(D-1)LR}$. For example, the vectors $\mathbf{m}_{UL}$ and $\mathbf{m}_{UL'}$ are

$$\mathbf{m}_{UL} = \mathbf{n}_{UDLR} - \mathbf{n}_{(U+1)D(L+1)R} \tag{4.33}$$

$$\mathbf{m}_{UL'} = \mathbf{n}_{(U-1)D(L-1)R} - \mathbf{n}_{UDLR} \tag{4.34}$$

The recursive method of the force analysis can now be realized by starting at the principal node. No primed members are present since only members that meet at this node come from the complexity above it. As long as an external force is applied to the tip, the equilibrium reduces to three equations and three unknowns, where the force in the members going into the node balances the externally applied force coming out of the node. Now that the force densities of the complexity 1 members are computed, the analysis moves to the second complexity. Now, there are three nodes to perform this force balance on. The forces in each node is independent of the others in its complexity, so the force analysis can be carried out individually. Generally, the forces in members coming out of any node will be known because of this recursive method. Therefore the forces of members coming *out of* the node are added together and are a "ficticious external force" that the unknown forces of each member going *into* the node must equate. Since the position of the nodes for cylindrical and spherical coordinates are different, this force analysis will be conducted and exemplified for both methods.

4.4.4 Forces at a General Node - Cylindrical Coordinates

Using cylindrical coordinates, the member vector of the first term in equation 4.32 is

$$\begin{aligned}\mathbf{m}_{UL} &= \mathbf{n}_{UDLR} - \mathbf{n}_{(U+1)D(L+1)R} \\ &= r_q \begin{bmatrix} \mathbb{X}\delta \\ \cos(\mathbb{Z}\phi) \\ \sin(\mathbb{Z}\phi) \end{bmatrix} - r_{l+1} \begin{bmatrix} (\mathbb{X}+1)\delta \\ \cos((\mathbb{Z}+1)\phi) \\ \sin((\mathbb{Z}+1)\phi) \end{bmatrix} \\ &= r_q \begin{bmatrix} \delta(\mathbb{X} - a - \mathbb{X}a) \\ c\cos(\mathbb{Z}\phi - \beta) \\ c\sin(\mathbb{Z}\phi - \beta) \end{bmatrix}\end{aligned}$$

Similarly

$$\mathbf{m}_{UR} = r_q \begin{bmatrix} \delta(\mathbb{X} + a - \mathbb{X}a) \\ c\cos(\mathbb{Z}\phi - \beta) \\ c\sin(\mathbb{Z}\phi - \beta) \end{bmatrix} \qquad \mathbf{m}_{D} = r_l \begin{bmatrix} \mathbb{X}\delta(1-a) \\ c\cos(\mathbb{Z}\phi + \beta) \\ c\sin(\mathbb{Z}\phi + \beta) \end{bmatrix}$$

The primed member vectors coming out of the node are

$$\mathbf{m}_{UL'} = r_{q-1} \begin{bmatrix} \delta(\mathbb{X} - 1 - \mathbb{X}a) \\ c\cos((\mathbb{Z}-1)\phi - \beta) \\ c\sin((\mathbb{Z}-1)\phi - \beta) \end{bmatrix} \quad \mathbf{m}_{UR'} = r_{q-1} \begin{bmatrix} \delta(\mathbb{X} + 1 - \mathbb{X}a) \\ c\cos((\mathbb{Z}-1)\phi - \beta) \\ c\sin((\mathbb{Z}-1)\phi - \beta) \end{bmatrix}$$

$$\mathbf{m}_{D'} = r_{q-1} \begin{bmatrix} \delta\mathbb{X}(1-a) \\ c\cos((\mathbb{Z}+1)\phi + \beta) \\ c\sin((\mathbb{Z}+1)\phi + \beta) \end{bmatrix}$$

By collecting the unknown, un-primed force densities into a vector, $\mathbf{X}^q = [\lambda_{UL}\ \lambda_{UR}\ \lambda_D]^T$ and the primed, known force densities into another vector, $\mathbf{X}^{q-1} = [\lambda_{UL'}\ \lambda_{UR'}\ \lambda_{D'}]^T$, a matrix linear algebra equation may be solved to compute the values of the unknown force densities. This equation begins in the form of:

$$\begin{bmatrix} \delta\left(\mathbb{X}-a-\mathbb{X}a\right) & \delta\left(\mathbb{X}+a-\mathbb{X}a\right) & \delta\mathbb{X}\left(1-a\right) \\ c\cos\left(\mathbb{Z}\phi-\beta\right) & c\cos\left(\mathbb{Z}\phi-\beta\right) & c\cos\left(\mathbb{Z}\phi+\beta\right) \\ c\sin\left(\mathbb{Z}\phi-\beta\right) & c\sin\left(\mathbb{Z}\phi-\beta\right) & c\sin\left(\mathbb{Z}\phi+\beta\right) \end{bmatrix} \mathbf{X}^{q} r_{q}$$

$$= \begin{bmatrix} \delta\left(\mathbb{X}-1-\mathbb{X}a\right) & \delta\left(\mathbb{X}+1-\mathbb{X}a\right) & \delta\mathbb{X}\left(1-a\right) \\ c\cos\left(\left(\mathbb{Z}-1\right)\phi-\beta\right) & c\cos\left(\left(\mathbb{Z}-1\right)\phi-\beta\right) & c\cos\left(\left(\mathbb{Z}+1\right)\phi+\beta\right) \\ c\sin\left(\left(\mathbb{Z}-1\right)\phi-\beta\right) & c\sin\left(\left(\mathbb{Z}-1\right)\phi-\beta\right) & c\sin\left(\left(\mathbb{Z}+1\right)\phi+\beta\right) \end{bmatrix} \mathbf{X}^{q-1} r_{q-1} + \mathbf{w} \tag{4.35}$$

Pre-multiplying by the inverse of the first matrix, and simplifying the result, we obtain an equation for the incoming members of a node for when $q \neq 0$:

$$\mathbf{X}^{q} r_{q} = \mathbf{C}\mathbf{X}^{q-1} r_{q-1} + \mathbf{A}^{-1}\mathbf{w} \tag{4.36}$$

$$\mathbf{C} = \frac{1}{2\sin\left(2\beta\right)} \begin{bmatrix} \sigma+\rho & h & h \\ g & \sigma-\rho & g \\ -2\sin\phi & -2\sin\phi & \sigma-\sin\phi \end{bmatrix} \tag{4.37}$$

$$\mathbf{A}^{-1} = \frac{1}{2ac\sin 2\beta} \begin{bmatrix} \frac{-c\sin\left(2\beta\right)}{\delta} & b_{s}^{-} & -b_{c}^{+} \\ \frac{-c\sin\left(2\beta\right)}{\delta} & b_{s}^{+} & -b_{c}^{-} \\ 0 & 2a\sin\left(\beta-\mathbb{Z}\phi\right) & 2a\cos\left(\beta-\mathbb{Z}\phi\right) \end{bmatrix} \tag{4.38}$$

$$\sigma = 2\sin\left(2\beta+\phi\right)+\sin\phi \tag{4.39}$$

$$\rho = \mathbb{X}\sin\left(2\beta\right)+\mathbb{X}\sin\left(2\beta 2\phi\right)-2\mathbb{X}\sin\left(2\beta+\phi\right) \tag{4.40}$$

$$h = \rho-\sin\phi \tag{4.41}$$

$$g = -\left(\rho+\sin\phi\right) \tag{4.42}$$

$$b_s^- = 2\mathbb{X}\cos(\mathbb{Z}\phi)\sin(\beta)(1-a) + a\sin(\mathbb{Z}\phi+\beta) \tag{4.43}$$

$$b_s^+ = 2\mathbb{X}\cos(\mathbb{Z}\phi)\sin(\beta)(a-1) + a\sin(\mathbb{Z}\phi+\beta) \tag{4.44}$$

$$b_c^- = 2\mathbb{X}\cos(\mathbb{Z}\phi)\sin(\beta)(1-a) + a\cos(\mathbb{Z}\phi+\beta) \tag{4.45}$$

$$b_c^+ = 2\mathbb{X}\cos(\mathbb{Z}\phi)\sin(\beta)(a-1) + a\cos(\mathbb{Z}\phi+\beta) \tag{4.46}$$

These equations provide a recursive form of solving for the force density of the members the entire truss, one complexity at a time. Beginning with the principal node, the members of each subsequent complexity are calculated by using a function of the truss' geometry and the parameters, $\mathbb{X}$ and $\mathbb{Z}$, derived from the indices of the current node of interest. Now, a similar formulation is done for the spherical coordinate parameterization.

4.4.5 Forces at a General Node - Spherical Coordinates

Given a general node $\mathbf{n}_{UDLR}$, in complexity level q, the three members coming *into* the nodes are $\mathbf{m}_{UL}$, $\mathbf{m}_{UR}$, $\mathbf{m}_D$ as described previously. Expanding equation 4.33,

$$\begin{aligned}
\mathbf{m}_{UL} &= \mathbf{n}_{UDLR} - \mathbf{n}_{(U+1)D(L+1)R} \\
&= r_l \begin{bmatrix} \cos(\mathbb{Z}\phi)\tan(\mathbb{X}\varepsilon) \\ \cos(\mathbb{Z}\phi) \\ \sin(\mathbb{Z}\phi) \end{bmatrix} - r_{l+1} \begin{bmatrix} \cos((\mathbb{Z}+1)\phi)\tan((\mathbb{X}+1)\varepsilon) \\ \cos((\mathbb{Z}+1)\phi) \\ \sin((\mathbb{Z}+1)\phi) \end{bmatrix} \\
&= r_l \begin{bmatrix} \cos(\mathbb{Z}\phi)\tan(\mathbb{X}\varepsilon) - a\cos((\mathbb{Z}+1)\phi)\tan((\mathbb{X}+1)\varepsilon) \\ \cos(\mathbb{Z}\phi) - a\cos((\mathbb{Z}+1)\phi) \\ \sin(\mathbb{Z}\phi) - a\sin((\mathbb{Z}+1)\phi) \end{bmatrix} \\
&= r_l \begin{bmatrix} \cos(\mathbb{Z}\phi)\tan(\mathbb{X}\varepsilon) - a\cos((\mathbb{Z}+1)\phi)\tan((\mathbb{X}+1)\varepsilon) \\ c * \cos(\mathbb{Z}\phi+\beta) \\ c * \sin(\mathbb{Z}\phi-\beta) \end{bmatrix}
\end{aligned}$$

similarly

$$\mathbf{m}_{UR} = r_l \begin{bmatrix} \cos(\mathbb{Z}\phi)\tan(\mathbb{X}\varepsilon) - a\cos((\mathbb{Z}+1)\phi)\tan((\mathbb{X}-1)\varepsilon) \\ c * \cos(\mathbb{Z}\phi + \beta) \\ c * \sin(\mathbb{Z}\phi - \beta) \end{bmatrix}$$

$$\mathbf{m}_{D} = r_l \begin{bmatrix} c * \tan(\mathbb{X}\varepsilon)\cos(\mathbb{X}\phi + \beta) \\ c * \cos(\mathbb{Z}\phi + \beta) \\ c * \sin(\mathbb{Z}\phi + \beta) \end{bmatrix}$$

Given node N_{UDLR} with externally applied force $\mathbf{w}_{UDLR}$, the force densities of the members coming into the node are collected into the vector $\mathbf{X}^q = [\lambda_{UL}\ \lambda_{UR}\ \lambda_D]^T$. Similarly, the force densities of the members coming out of the node are $\mathbf{X}^{q-1} = [\lambda_{UL'}\ \lambda_{UR'}\ \lambda_{D'}]^T$. The force equilibrium of the node is composed of the following matrix equation

$$\mathbf{A}\mathbf{X}^q r_q = \mathbf{B}\mathbf{X}^{q-1} r_{q-1} + \mathbf{w}_{UDLR} \tag{4.47}$$

$$\mathbf{A} = \begin{bmatrix} g & h & c\tan(\mathbb{X}\varepsilon)\cos(\mathbb{Z}\phi+\beta) \\ c\cos(\mathbb{Z}\phi+\beta) & c\cos(\mathbb{Z}\phi+\beta) & c\cos(\mathbb{Z}\phi+\beta) \\ c\sin(\mathbb{Z}\phi-\beta) & c\sin(\mathbb{Z}\phi-\beta) & c\sin(\mathbb{Z}\phi+\beta) \end{bmatrix} \tag{4.48}$$

$$\mathbf{B} = \begin{bmatrix} g' & h' & c\cos((\mathbb{Z}+1)\phi+\beta)\tan(\mathbb{X}\varepsilon) \\ c\cos((\mathbb{Z}-1)\phi-\beta) & c\cos((\mathbb{Z}-1)\phi-\beta) & c\cos((\mathbb{Z}+1)\phi+\beta) \\ c\sin((\mathbb{Z}-1)\phi-\beta) & c\sin((\mathbb{Z}-1)\phi-\beta) & c\sin((\mathbb{Z}+1)\phi+\beta) \end{bmatrix} \tag{4.49}$$

$$g = \cos(\mathbb{Z}\phi)\tan(\mathbb{X}\varepsilon) - a\cos((\mathbb{Z}+1)\phi)\tan((\mathbb{X}+1)\varepsilon) \tag{4.50}$$

$$h = \cos(\mathbb{Z}\phi)\tan(\mathbb{X}\varepsilon) - a\cos((\mathbb{Z}+1)\phi)\tan((\mathbb{X}-1)\varepsilon) \tag{4.51}$$

$$g' = \cos((\mathbb{Z}-1)\phi)\tan((\mathbb{X}-1)\varepsilon) - a\cos(\mathbb{Z}\phi)\tan(\mathbb{X}\varepsilon) \tag{4.52}$$

$$h' = \cos((\mathbb{Z}-1)\phi)\tan((\mathbb{X}+1)\varepsilon) - a\cos(\mathbb{Z}\phi)\tan(\mathbb{X}\varepsilon) \tag{4.53}$$

The matrix $\mathbf{A}$ is then inverted and pre-multiplied to both sides to achieve an equation for the force densities of each incoming member.

4.5 Minimum Material Volume

Once the force density of each member is calculated, it is possible to determine the minimum cross-sectional area of each member necessary to support the calculated stress, assuming some chosen material. Along with the stress of the member, the mass of the member will be dependent on the material density of the bars and strings. Since the members are assumed to experience only uni-axial forces, failure by bending is not applicable to these members. Thus, the failure modes that are expected of these members are failure by yielding or failure by buckling [61]. Of course, since strings cannot support compression loads, they will only fail by yielding.

Consider the 3D Michell truss with α strings and β bars. Assume all strings are of the same material of density ρ_s with yield strength σ_{sY}, and all bars are made of the same material (but possibly different than the strings) of density ρ_b with yield stress σ_{bY} and modulus of elasticity, E_b. Then, the minimum mass for the k^{th} string, of length s_k, to support a tensile force density, γ_k, assuming failure by yielding is

$$^{k}m_s = \frac{\rho_s}{\sigma_{sY}}\gamma_k s_k^2 \tag{4.54}$$

Assuming a constant cross-sectional area of the string, the minimum radius of the k^{th} string is

$$^{k}r_s = \sqrt{\frac{\gamma_k s_k}{\pi \sigma_{sY}}} \tag{4.55}$$

The calculation of the minimum mass of the k^{th} bar of length b_k experiecing a force density of λ_k is dependent on the failure mode. The mass for yielding, $^{k}m_{bY}$, and buckling, $^{k}m_{bB}$ are

$$^{k}m_{bY} = \frac{\rho_b}{\sigma_{bY}}\lambda_k b_k^2 \tag{4.56}$$

$$^{k}m_{bB} = 2\rho_b b_k^2 \sqrt{\frac{\lambda_k b_k}{\pi E_b}} \tag{4.57}$$

The corresponding member radius to support yielding and buckling are, respectively

$$ {}^{k}r_{bY} = \sqrt{\frac{\lambda_k b_k}{\pi \sigma_{bY}}} \tag{4.58} $$

$$ {}^{k}r_{bB} = \left(\frac{4\lambda_k b_k^3}{\pi^3 E_b} \right)^{\left(\frac{1}{4}\right)} \tag{4.59} $$

To ensure the bars will not fail either by yielding or buckling, the optimal radius for both modes should be computed and the maximum of the two chosen for the design. Thus, the minimum material volume of the 3D Truss is the sum of all members' volume.

$$ V = V_b + V_s \tag{4.60} $$

$$ V = \sum_{i=1}^{\beta} \pi^i r_b^2 b_i + \sum_{j=1}^{\alpha} \pi^j r_s^2 s_j \tag{4.61} $$

The total mass of the 3D truss is compared to that of the 2D truss ($\delta = 0$) given a single bending load in the $-\hat{\imath}_2$ direction for $\delta = [0.1,\ 0.25,\ 0.5]$ and a range of complexity from $[2, 35]$. The other geometric parameters of the 2D and 3D michell truss are $r_0 = 1,\ \beta = \frac{\pi}{6},\ \phi = \frac{\pi}{q}$. The results of this comparison are shown in figure 4.18.

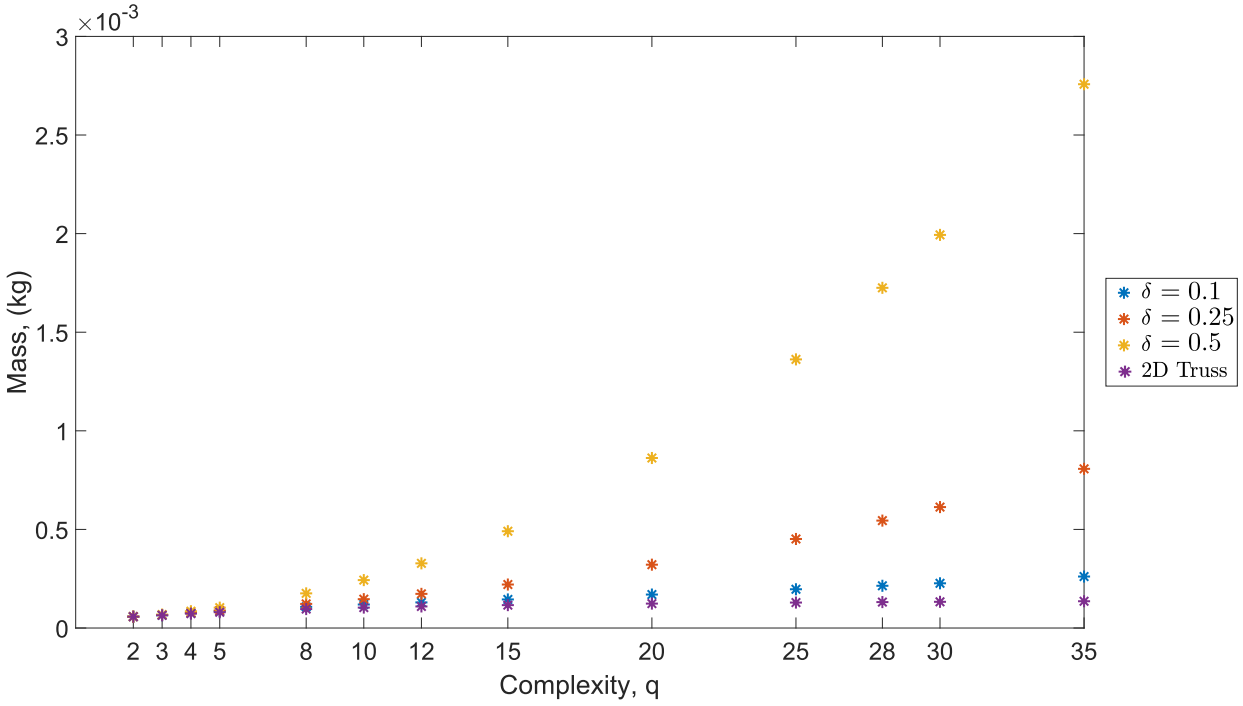

Figure 4.18: Mass of 2D and 3D truss, $\delta = [0, 0.1,\ 0.25,\ 0.5]$

The mass of the truss is comparative for complexity $q < 5$. However, as the complexity increases further, the mass of the 3D truss begins to diverge from the planar truss. Given the choice of δ as a static value, the extension out of the plane is unconstrained. Additionally, as the complexity increases, the force density of the members in the higher complexity increases. For the 2D truss, the increase of force density from this phenomina is countered by a decrease in these member lengths such that the total mass is unaffected. This quality is not exhibited by the 3D truss and is exacerbated as δ increases.

4.5.1 Example: Minimum Material Volume for a Complexity 1 Truss

Consider a 3D Michell truss parameterized by cylindrical coordinates as described in section 4.3.2 experiencing a single bending load of magnitude w_0 at the tip such that $\varphi = 0$ and $\gamma = \pi$. The force density of each member under a single bending load at the tip under this condition is derived in section 4.4.1. The positive sign of λ_{1010} and λ_{1001} indicates that those members are in tension while member $\mathbf{m}_{0100}$ undergoes compression. Thus for this example, members $\mathbf{m}_{1010}$ and

$\mathbf{m}_{1001}$ are strings and member $\mathbf{m}_{0100}$ is a bar. Each string experiences the same stress and is of the same material. Thus, the minimum radius of the strings is calculated by substituting (4.18) into (4.55)

$$r_{1010} = r_{1001} = \sqrt{\frac{w_0 \|\mathbf{m}_{1010}\|}{4\pi\sigma_{sY} r_0 c \sin\beta}} \tag{4.62}$$

$$\|\mathbf{m}_{1010}\| = r_1\left(\delta^2 + c^2\right)$$

Now, the minimum radius for both failure modes is calculated for the bar member by substituting equation 4.20 into equations 4.58 and 4.59

$$Yielding:\ r_{0100_Y} = \sqrt{\frac{w_0 \|\mathbf{m}_{0100}\|}{2\pi\sigma_{bY} r_0 c \sin\beta}} \tag{4.63}$$

$$Buckling:\ r_{0100_B} = \left(\frac{2w_0 \|\mathbf{m}_{0100}\|^3}{\pi^3 E_b r_0 c \sin\beta}\right)^{\left(\frac{1}{4}\right)} \tag{4.64}$$

$$\|\mathbf{m}_{0100}\| = r_1 c$$

It is interesting to note that, by comparing equations 4.63 and 4.64, an inequality can be derived to determine what failure mode is expected accoring to the material properties and design parameters. As mentioned previously, it is expected for a bar member to fail by buckling if $r_{bB} > r_{bY}$. This inequality is true if

$$r_0 r_1 c^2 \sin\beta > \frac{\pi w_0 E_b}{8\sigma_{bY}^2} \tag{4.65}$$

Finally, the total material volume for the complexity 1 truss is

$$V = V_b + V_s \tag{4.66}$$

$$= \pi\left(\max\left[r_{0100_Y}^2, r_{0100_B}^2\right] r_1 c + 2r_{1010}^2 r_1\left(\delta^2 + c^2\right)\right) \tag{4.67}$$

Recall that r_1 in this context is the radius of the cylinder to which the truss is pinned, not the radius of a member.

4.6 Additional Strings

Similar to the 3-bar wheel, including extra strings in the 3D Michell's topology can change the behavior of its response to an external load. The method of adding extra strings in this work places strings along each sub-triangle that is formed in each complexity. A complexity 1 truss needs no strings since the members are already pinned to the base, so this string rule is established only for trusses of complexity $q > 2$. An example of this rule is shown for complexity 2 and 3 trusses in figure 4.19 below. In this figure, the blue members are members of the original truss and the red members are the additional strings. The complexity 2 truss has a single set of additional strings that are placed between nodes 2 and 3, 3 and 4, and 2 and 4. The complexity 3 truss adds three additional sets.

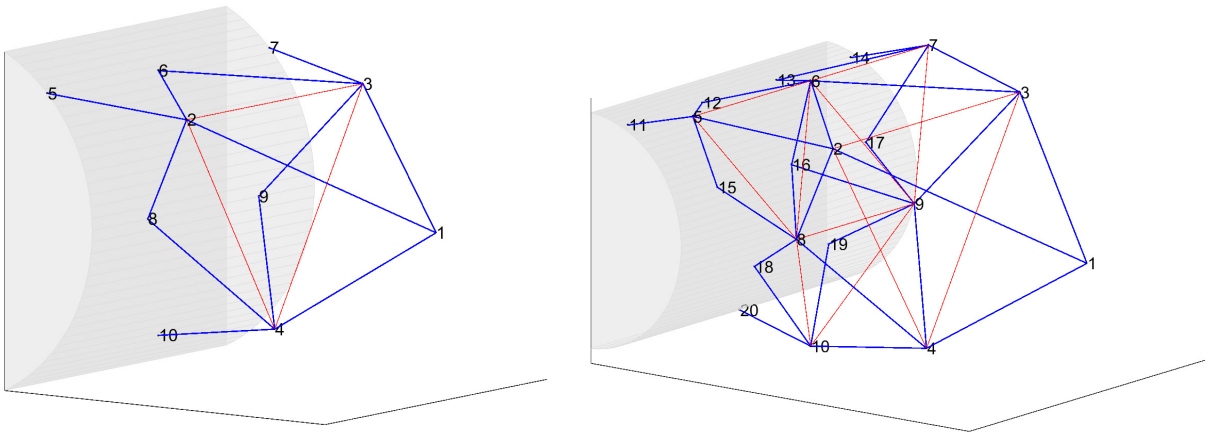

Figure 4.19: Extra Strings on 3D Michell Truss of Complexity 2 and 3

The utility of these strings is the ability to reduce the variability of force density sign in many of the members as the direction of the external force changes. If the tension in the extra strings is sufficiently high, the members in all complexities beyond the first complexity maintain their initial sign. An example for a complexity 2 truss for a range of γ between $[0, 2\pi]$ was conducted to represent this utility. It is important to note that this is still a static investigation. In other words, static equilibrium is conducted for the given range of γ. The top plot of Figure 4.20 is the result

for a truss with no additional strings. The bottom plot is the result of adding strings with sufficient tension such that the external force does not dominate the response of the truss.

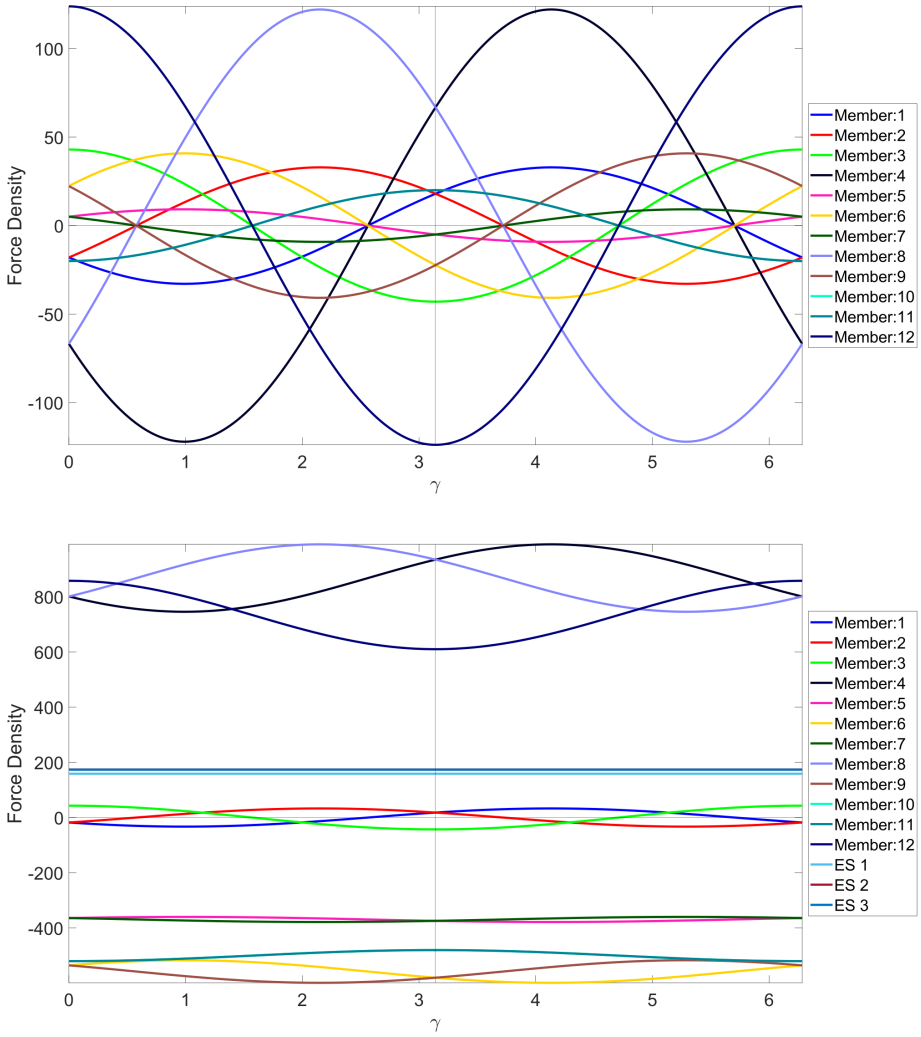

Figure 4.20: Force Density of Members. Top: low pre-stress; Bottom: high pre-stress

By adding additional members, the range of operability of a given configuration is widened such that all members except for the front members do not change sign. Adding members by different methods, in conjunction with replacing bars with strings and vice-versa, may provide a more mass optimized truss than presented herein, which will be the focus of future research effort.

4.7 Concluding Remarks

This chapter reviews the discrete Michell truss introduced by Skelton [1], and presents a novel topology that extends this planar truss into 3-D space. A comprehensive force analysis at a general node is provided and analytical solutions for the member forces of complexity 1 topologies are explored. The results of the examples provided are a mapping of the expected sign of the force for the three members as a function of the direction of external bending load. By adding additional strings, the status of compression or tension for all but the three tip members is maintained. Finally, minimum material volume to support a given external load according to yield or buckling failure is presented with an analytical example for a complexity 1 topology. The total mass of the 3D truss is compared to that of the planar truss for discrete values of δ. The results show comparable mass for low complexities ($q \leq 5$), but divergence of mass from the planar truss for higher complexities.

5. THE 3D T-BAR WHEEL

The discrete Michell truss is the optimal tensegrity topology to resist bending loads, however this optimality exists only for certain directions of the force. Based on this direction, there are regions that members may be pre-assigned either bar or string to support that load at peak mass efficiency. Relating back to the application of using this as a wheel, it falls short since the forces applied may be outside that design envelope. Specifically, the wheel may be well designed for rolling forward, but what if it must rotate backwards? The truss would not be able to support the bending load from that direction, and it would immediately collapse. So, the question then arises: how can this 3D truss be modified to accept a bending load from all directions? The objective of this chapter is to present a prototypical structure to answer this question, however no analysis is provided.

5.1 The T-Bar

An alternative structure that ensures the compressive member will stay in compression, and experience minimal bending moment is desired. Similar to the 3-bar wheel discussed in chapter 3, the T-Bar wheel is designed by iterating a base prism in a loop. Since this prism is based off the 3D Michell, it follows that it must be rigidly joined to a base cylinder. Consequently, this new wheel will require a traditional rim. This prism modifies the original three point configuration of the 3D Michell truss to a four point configuration. This is done by redefining the node parameterization so that the next order of nodes is made of four 'offspring' nodes that update the index by

1. U+1; L+1

2. U+1; R+1

3. D+1; L+1

4. D+1; R+1

So the four nodes to create a complexity 1 truss for the wheel of this configuration are

$$\mathbf{n}_{1010} = r(1) * \begin{bmatrix} \delta \\ \cos(\phi) \\ \sin(\phi) \end{bmatrix} \quad \mathbf{n}_{1001} = r(1) * \begin{bmatrix} -\delta \\ \cos(\phi) \\ \sin(\phi) \end{bmatrix}$$

$$\mathbf{n}_{0110} = r(1) * \begin{bmatrix} \delta \\ \cos(-\phi) \\ \sin(-\phi) \end{bmatrix} \quad \mathbf{n}_{0101} = r(1) * \begin{bmatrix} -\delta \\ \cos(-\phi) \\ \sin(-\phi) \end{bmatrix}$$

Each member of the truss is designated to be a string and then a bar is attached on the radial line from the rim to the principal node, shown in figure 5.1. What is formed is actually another type of tensegrity prism called a T-Bar [12], however the truss is formed using the parameters defined by the 3D Michell. The advantage of this configuration over the three-point Michell truss comes from the tension in the strings always forcing the rod to be in compression. Thus, an external force can always be supported by at least the rod and two of the strings, dependent on the direction of the force.

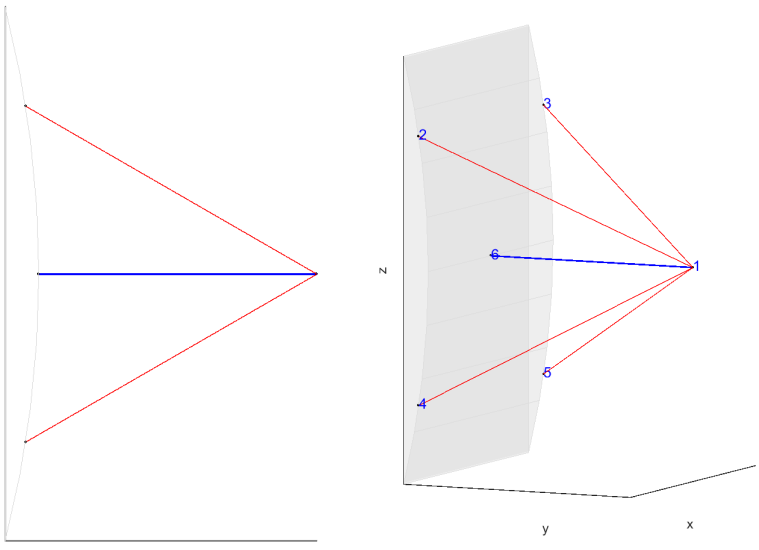

Figure 5.1: Single Tread of T-Bar Wheel

Repeating this truss in a loop constructs the entire wheel.

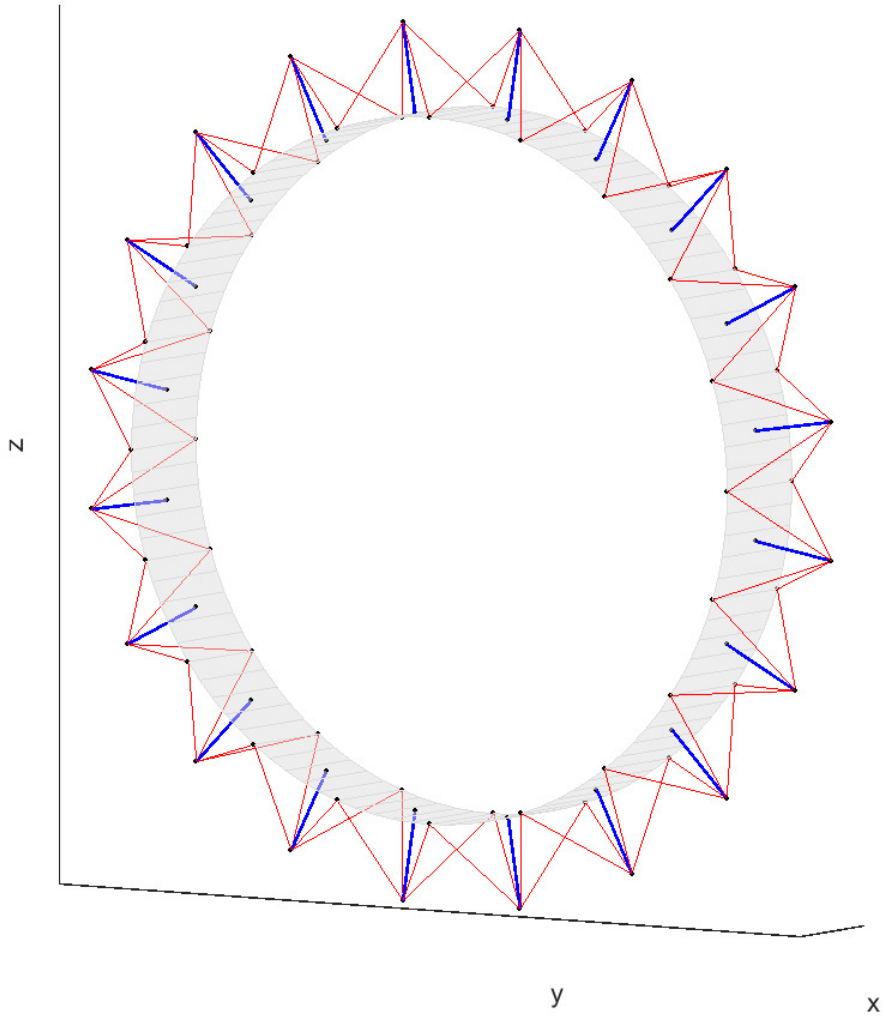

Figure 5.2: T-Bar Wheel

Now, this current configuration is unstable in the $\hat{\imath}_2, \hat{\imath}_3$ plane. This can be resolved by translating a copy of this loop in the $\hat{\imath}_1$ direction such that there are now four contact points with the ground while standing still.

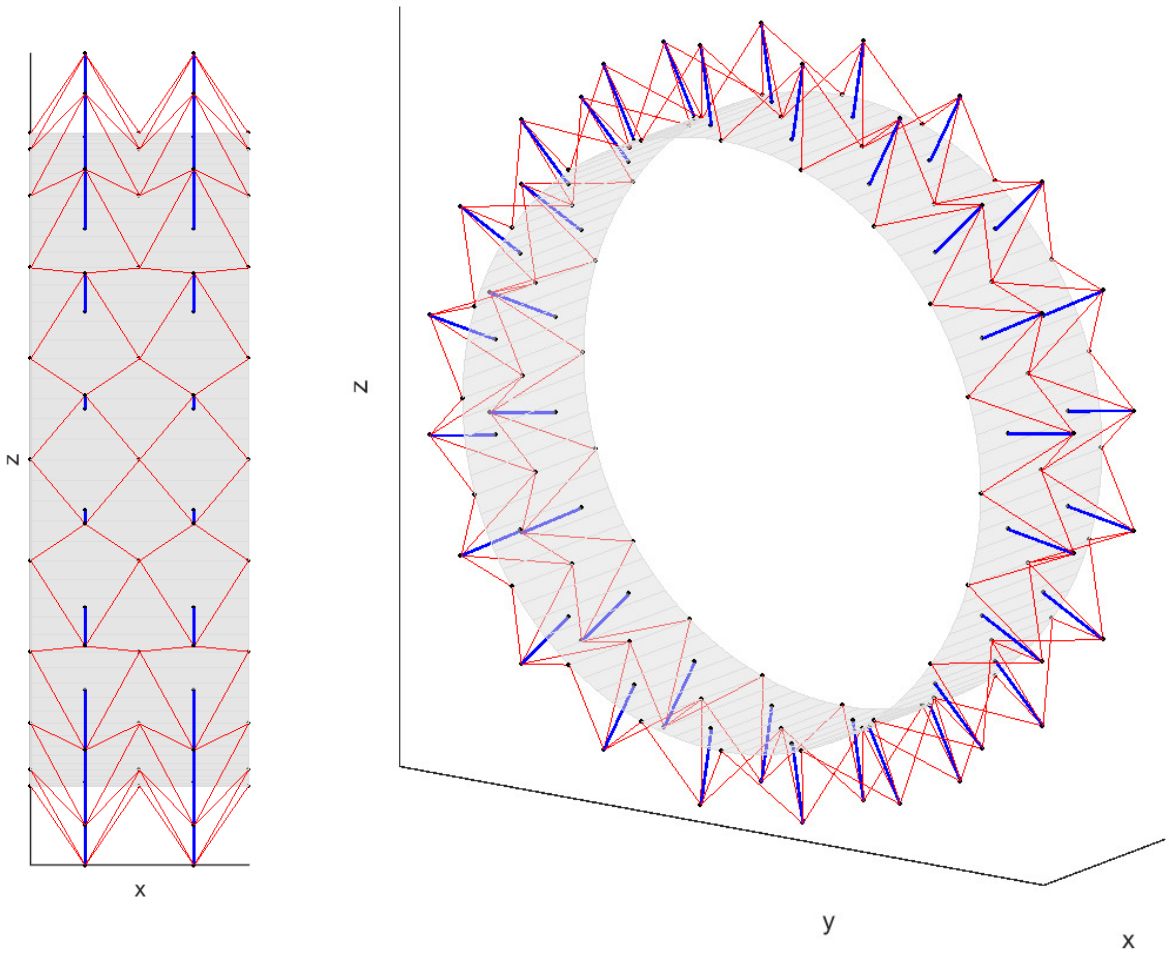

Figure 5.3: Extended T-Bar Wheel

The wheel's tread is perpendicular to the ground, thus the out-of-plane stability is still lacking. However, if this wheel is used on a vehicle, the out of plane forces will be resisted by the vehicle itself. Then, the sharp angle of the tread to the ground would allow the tread to 'dig' into a soft terrain and provide exceptional traction over a typical wheel that may use grousers to obtain traction. Additionally, the design of the tensegrity structure ensures the bar will always maintain compression, therefore the durability of the tread will be better than a grouser that experiences stressful bending moments.

6. FINAL SUMMARY

Two major contributions have been presented in this thesis. First, a novel tensegrity toroid based on the three-bar prism has been designed. A dynamic model was created to simulate the toroid rolling like wheel across a surface, with a focus on what parameters contribute to how smooth the wheel rolls. Results of these simulations confirm the theory that higher complexity and a wider tread will improve rolling stability over firm ground. Second, the planar Michell truss was extended out of the plane and a new 3D Michell truss was designed and analyzed. This new truss incorporates a different indexing scheme than the planar truss, along with two methods of parameterizing the out-of-plane locations. Comprehensive force analysis offers a recursive method for determining the forces in each member is shown and minimum material volume calculations were also performed, with analytical examples for a complexity 1 truss. The parameters describing this truss was used to form a T-bar which attaches to a rigid rim to form the tread for what is considered a prototype T-bar wheel. The structures presented herein expand the working design envelope for toroidal tensegrity structures and forms a foundation for further research and application to be applied.

REFERENCES

[1] R. E. Skelton and M. C. de Oliveira, "Optimal tensegrity structures in bending: The discrete michell truss," *Journal of the Franklin Institute*, vol. 347, no. 1, pp. 257–283, 2010.

[2] V. Gomez Jauregui, "Controversial origins of tensegrity," in *Symposium of the International Association for Shell and Spatial Structures (50th. 2009. Valencia). Evolution and Trends in Design, Analysis and Construction of Shell and Spatial Structures: Proceedings*, Editorial Universitat Politècnica de València, 2009.

[3] M. Gough, *The artist as producer: Russian constructivism in revolution*. Univ of California Press, 2005.

[4] K. D. Snelson, "Continuous tension, discontinuous compression structures," Feb. 16 1965. US Patent 3,169,611.

[5] K. Snelson, "The art of tensegrity," *International journal of space structures*, vol. 27, no. 2-3, pp. 71–80, 2012.

[6] C. Sultan, "Tensegrity: 60 years of art, science, and engineering," *Advances in applied mechanics*, vol. 43, pp. 69–145, 2009.

[7] C. Calladine, "Buckminster fuller's "tensegrity" structures and clerk maxwell's rules for the construction of stiff frames," *International Journal of Solids and Structures*, vol. 14, no. 2, pp. 161–172, 1978.

[8] H. Lalvani, "Origins of tensegrity: views of emmerich, fuller and snelson," *International Journal of Space Structures*, vol. 11, no. 1-2, pp. 27–27, 1996.

[9] C. Sultan, M. Corless, and R. E. Skelton, "The prestressability problem of tensegrity structures: some analytical solutions," *International Journal of Solids and Structures*, vol. 38, no. 30-31, pp. 5223–5252, 2001.

[10] C. Sultan and R. Skelton, "Tensegrity structures prestressability investigation," *International Journal of Space Structures*, vol. 18, no. 1, pp. 15–30, 2003.

[11] S. H. Juan and J. M. M. Tur, "Tensegrity frameworks: Static analysis review," *Mechanism and Machine Theory*, vol. 43, no. 7, pp. 859–881, 2008.

[12] R. E. Skelton and M. C. de Oliveira, *Tensegrity systems*, vol. 1. Springer, 2009.

[13] F. R. Buckminster, "Tensile-integrity structures," Nov. 13 1962. US Patent 3,063,521.

[14] A. Pugh, *An introduction to tensegrity*. Univ of California Press, 1976.

[15] R. Motro, S. Najari, and P. Jouanna, "Static and dynamic analysis of tensegrity systems," in *Shell and Spatial Structures: Computational Aspects*, pp. 270–279, Springer, 1987.

[16] R. Motro, "Structural morphology of tensegrity systems," *International Journal of Space Structures*, vol. 11, no. 1-2, pp. 233–240, 1996.

[17] R. Motro, *Tensegrity: structural systems for the future*. Elsevier, 2003.

[18] R. T. Skelton and C. Sultan, "Controllable tensegrity: a new class of smart structures," in *Smart structures and materials 1997: mathematics and control in smart structures*, vol. 3039, pp. 166–177, International Society for Optics and Photonics, 1997.

[19] C. Sultan and R. Skelton, "Deployment of tensegrity structures," *International Journal of Solids and Structures*, vol. 40, no. 18, pp. 4637–4657, 2003.

[20] K. Nagase and R. Skelton, "Network and vector forms of tensegrity system dynamics," *Mechanics Research Communications*, vol. 59, pp. 14–25, 2014.

[21] D. E. Ingber, "Tensegrity: the architectural basis of cellular mechanotransduction," *Annual review of physiology*, vol. 59, no. 1, pp. 575–599, 1997.

[22] C. Sultan and R. Skelton, "A force and torque tensegrity sensor," *Sensors and Actuators A: Physical*, vol. 112, no. 2-3, pp. 220–231, 2004.

[23] S. Djouadi, R. Motro, J. Pons, and B. Crosnier, "Active control of tensegrity systems," *Journal of Aerospace Engineering*, vol. 11, no. 2, pp. 37–44, 1998.

[24] C. Sultan and R. T. Skelton, "Tendon control deployment of tensegrity structures," in *Smart Structures and Materials 1998: Mathematics and Control in Smart Structures*, vol. 3323, pp. 455–466, International Society for Optics and Photonics, 1998.

[25] N. Veuve, S. D. Safaei, and I. F. Smith, "Deployment of a tensegrity footbridge," *Journal of Structural Engineering*, vol. 141, no. 11, p. 04015021, 2015.

[26] A. Tibert and S. Pellegrino, "Deployable tensegrity reflectors for small satellites," *Journal of Spacecraft and Rockets*, vol. 39, no. 5, pp. 701–709, 2002.

[27] G. Tibert, *Deployable tensegrity structures for space applications*. PhD thesis, KTH, 2002.

[28] B. Roth and W. Whiteley, "Tensegrity frameworks," *Transactions of the American Mathematical Society*, vol. 265, no. 2, pp. 419–446, 1981.

[29] R. Motro, "Tensegrity systems: the state of the art," *International journal of space structures*, vol. 7, no. 2, pp. 75–83, 1992.

[30] C. Sultan, M. Corless, and R. E. Skelton, "Symmetrical reconfiguration of tensegrity structures," *International Journal of Solids and Structures*, vol. 39, no. 8, pp. 2215–2234, 2002.

[31] R. Motro, "Structural morphology of tensegrity systems," *Meccanica*, vol. 46, no. 1, pp. 27–40, 2011.

[32] H. Murakami and Y. Nishimura, "Static and dynamic characterization of regular truncated icosahedral and dodecahedral tensegrity modules," *International Journal of Solids and Structures*, vol. 38, no. 50-51, pp. 9359–9381, 2001.

[33] C. Sultan, M. Corless, and R. T. Skelton, "Peak-to-peak control of an adaptive tensegrity space telescope," in *Smart Structures and Materials 1999: Mathematics and Control in Smart Structures*, vol. 3667, pp. 190–201, International Society for Optics and Photonics, 1999.

[34] F. Fu, "Structural behavior and design methods of tensegrity domes," *Journal of Constructional Steel Research*, vol. 61, no. 1, pp. 23–35, 2005.

[35] X. Yuan, Z. Peng, S. Dong, and B. Zhao, "A new tensegrity module—"torus"," *Advances in structural engineering*, vol. 11, no. 3, pp. 243–251, 2008.

[36] X. Xu, S. Li, and Y. Luo, "Form-finding of a new kind of tensegrity tori using overlapping modules," *Mechanics Research Communications*, vol. 84, pp. 1–7, 2017.

[37] K. Nagase and R. Skelton, "Double-helix tensegrity structures," *Aiaa Journal*, vol. 53, no. 4, pp. 847–862, 2015.

[38] J. Lu, X. Dong, X. Zhao, X. Wu, and G. Shu, "Form-finding analysis for a new type of cable–strut tensile structures generated by semi-regular tensegrity," *Advances in Structural Engineering*, vol. 20, no. 5, pp. 772–783, 2017.

[39] M. P. Bendsoe and N. Kikuchi, "Generating optimal topologies in structural design using a homogenization method," 1988.

[40] H. Jones, "The recent large reduction in space launch cost," 48th International Conference on Environmental Systems, 2018.

[41] B. K. Muirhead, "Mars rovers, past and future," in *2004 IEEE aerospace conference proceedings (IEEE Cat. No. 04TH8720)*, vol. 1, IEEE, 2004.

[42] N. C. Costes, J. E. Farmer, and E. B. George, *Mobility Performance of the Lunar Roving Vehicle: Terrestrial Studies, Apollo 15 Results*, vol. 401. NASA, 1972.

[43] V. Asnani, D. Delap, and C. Creager, "The development of wheels for the lunar roving vehicle," *Journal of Terramechanics*, vol. 46, no. 3, pp. 89–103, 2009.

[44] D. Shirley and J. Matijevic, "Mars pathfinder microrover," *Autonomous Robots*, vol. 2, no. 4, pp. 283–289, 1995.

[45] A. H. Mishkin, J. C. Morrison, T. T. Nguyen, H. W. Stone, B. K. Cooper, and B. H. Wilcox, "Experiences with operations and autonomy of the mars pathfinder microrover," in *1998 IEEE aerospace conference proceedings (Cat. No. 98TH8339)*, vol. 2, pp. 337–351, IEEE, 1998.

[46] R. Roncoli and J. Ludwinski, "Mission design overview for the mars exploration rover mission," in *AIAA/AAS Astrodynamics Specialist Conference and Exhibit*, p. 4823, 2002.

[47] T. Flessa, E. W. McGookin, and D. G. Thomson, "Taxonomy, systems review and performance metrics of planetary exploration rovers," in *2014 13th International Conference on Control Automation Robotics & Vision (ICARCV)*, pp. 1554–1559, IEEE, 2014.

[48] N. Patel, R. Slade, and J. Clemmet, "The exomars rover locomotion subsystem," *Journal of Terramechanics*, vol. 47, no. 4, pp. 227–242, 2010.

[49] D. Cardile, N. Viola, S. Chiesa, and A. Rougier, "Applied design methodology for lunar rover elastic wheel," *Acta Astronautica*, vol. 81, no. 1, pp. 1–11, 2012.

[50] G. Sharma, S. Tiwary, A. Kumar, H. S. Kumar, and K. K. Murthy, "Systematic design and development of a flexible wheel for low mass lunar rover," *Journal of Terramechanics*, vol. 76, pp. 39–52, 2018.

[51] L. Ding, H. Gao, Z. Deng, K. Nagatani, and K. Yoshida, "Experimental study and analysis on driving wheels' performance for planetary exploration rovers moving in deformable soil," *Journal of Terramechanics*, vol. 48, no. 1, pp. 27–45, 2011.

[52] J. Zheng, H. Gao, B. Yuan, Z. Liu, H. Yu, L. Ding, and Z. Deng, "Design and terramechanics analysis of a mars rover utilising active suspension," *Mechanism and Machine Theory*, vol. 128, pp. 125–149, 2018.

[53] R. Goyal, M. Chen, M. Majji, and R. Skelton, "Motes: Modeling of tensegrity structures," *Journal of Open Source Software*, vol. 4, no. 42, p. 1613, 2019.

[54] R. Goyal and R. E. Skelton, "Tensegrity system dynamics with rigid bars and massive strings," *Multibody System Dynamics*, vol. 46, no. 3, pp. 203–228, 2019.

[55] A. A. Shabana, *Dynamics of multibody systems*. Cambridge university press, 2003.

[56] M. Masic and R. E. Skelton, "Open-loop control of class-2 tensegrity towers," in *Smart Structures and Materials 2004: Modeling, Signal Processing, and Control*, vol. 5383, pp. 298–308, International Society for Optics and Photonics, 2004.

[57] H. Liu, J. Zhang, and M. Ohsaki, "New 3-bar prismatic tensegrity units," *Composite Structures*, vol. 184, pp. 306–313, 2018.

[58] M. C. de Oliveira, R. E. Skelton, and W. Chan, "Minimum mass design of tensegrity towers and plates," in *Proceedings of the 45th IEEE Conference on Decision and Control*, pp. 2314–2319, IEEE, 2006.

[59] A. G. M. Michell, "Lviii. the limits of economy of material in frame-structures," *The London, Edinburgh, and Dublin Philosophical Magazine and Journal of Science*, vol. 8, no. 47, pp. 589–597, 1904.

[60] G. I. Rozvany, "Some shortcomings in michell's truss theory," *Structural optimization*, vol. 12, no. 4, pp. 244–250, 1996.

[61] G. Carpentieri, R. E. Skelton, and F. Fraternali, "Parametric design of minimal mass tensegrity bridges under yielding and buckling constraints," *arXiv:1411.7966*, 2014.